N-symmetric interaction of N hetons. Part I: Analysis of the case $N = 2$

M.A. Sokolovskiy[1,2,a], K.V. Koshel[3,4], D.G. Dritschel[5], J.N. Reinaud[5]

[1] Water Problems Institute of RAS, 3, Gubkina Str., 119333, Moscow, Russia

[2] Shirshov Institute of Oceanology of RAS 36, Nahimovsky Prosp., 117997, Moscow, Russia

[3] Pacific Oceanological Institute of FEB RAS, 43, Baltiyskaya Str., 690041, Vladivostok, Russia

[4] Institute of Applied Mathematics of FEB RAS, 7, Radio Str., 690022, Vladivostok, Russia

[5] Mathematical Institute, University of St Andrews, North Haugh, St Andrews KY16 9SS, United Kingdom

[a] Author to whom correspondence should be addressed: sokolovskiy@iwp.ru

August 11, 2020

Abstract

We examine the motion of N symmetric hetons (opposite-signed vertical dipoles) in a two-layer quasi-geostrophic model. We consider the special case of N-fold symmetry in which the original system of $4N$ ordinary differential equations reduces to just two equations for the so-called 'equivalent' heton. We perform a qualitative analysis to classify the possible types of vortex motions for the case $N = 2$. We identify the regions of the parameter space corresponding to unbounded motion and to different types of bounded, or localized, motion. We focus on the properties of localized, in particular periodic, motion. We identify classes of absolute and relative 'choreographies' first introduced by [C. Simó, New families of solutions to the N-body problems, Progr. Math series, vol. 201, 101 (2001)]. We also study the forms of the vortex trajectories occurring for unbounded motion, which are of practical interest due to the associated transport of heat and mass over large distances.

Introduction

The concept of 'heton' (derived from the word 'heat') was first introduced by Hogg and Stommel in [31] for a vortex structure consisting of two oppositely-signed point vortices located in different layers of a two-layer rotating fluid. This is the simplest model of a baroclinic vortex which can transport heat. Indeed, due to geostrophic and hydrostatic balance in a rotating two-layer fluid, the cyclonic vortex in the upper layer and the anticyclonic vortex in the lower layer both initiate local uplifts of the interface between the layers. This means that the liquid column surrounding the vortices is colder than any other column (in a stable stratification, the lower layer is colder than the upper layer). Thus, a heton consisting of a cyclone in the upper layer and an anticyclone in the lower layer is called a cold heton. When the vorticity signs of both vortices change, it is a warm heton. Obviously, when such a vortex structure moves, it transports heat in the horizontal direction.

The general equations of motion of point vortices in a two-layer quasi-geostrophic fluid were first obtained by Gryanik in [21], and have been subsequently used in many studies. A

sample of the vast literature can be found in [22, 23, 31, 32, 34, 35, 65–70, 78]. Further work has generalised point vortices to distributed ones, often (and most simply) vortex patches having uniform potential vorticity. Various aspects of distributed-heton dynamics have been investigated in [30, 38, 44, 49–53, 56, 60–62, 65, 68, 72–77].

It is feasible to generate hetons in laboratory experiments, either by using sources and sinks of mass [19, 20], by the mechanical rotation of the upper layer [57, 71], or by using heat or buoyancy sources [17, 18, 29]. In Nature, particularly in the oceans, such vortices may arise from the instability of baroclinic currents [47], from the formation of fresh water pools during sea-ice melting [8–10], and from deep convection in the ocean [16, 36, 39, 41–43].

The heton model has been applied in remarkably diverse ways. For example, it has been used to study the stability of clouds [48], idealised features of tropical cyclones and hurricanes [45, 46], Mediterranean intra-thermocline lenses [33], horizontal heat and passive admixture transfer in the ocean [26–28, 40], the destruction of cyclonic vortex structures above sloping topography [11] or over canyons under ice [12, 58], and the baroclinic von Kármán vortex street [24, 25]. Hetons are likely to make a significant contribution to heat transport in the oceans, and the results presented here explain one of the ways this may occur.

The paper is organized as follows. Section 1 presents the mathematical model and formulates the general problem for the motion of an N heton system, i.e. $2N$ vortices in a two-layer quasi-geostrophic fluid. Section 2 then restricts the problem to N-fold symmetry, thereby reducing the original system of $4N$ equations to 4 equations for the motion of an 'equivalent' heton. Section 3 uses conservation of angular momentum and a further symmetry to reduce the system to only 2 equations for the so-called 'virtual' vortex. The main results — obtained using the maximally-reduced model — are described in Section 4, followed by conclusions in Section 5.

1 Mathematical model and problem formulation

We employ the two-layer quasi-geostrophic model to study the motion of systems of $2N$ point vortices. We assume for simplicity that the layers have equal thickness, with dimensionless thicknesses $h_1 = h_2 = 1/2$. Each layer is assumed to contain N identical vortices, located initially at the vertices of a regular N-gon. The vortices in the layers are taken to have opposite strengths (volume integrated potential vorticity), so that the net integrated potential vorticity is zero. The regular N-gons possess a common centre, but can have different face lengths (or radii of the circles they lie on). Additionally, we allow for the two N-gons to be offset, angularly, while of course maintaining equal angular separation ($= 2\pi/N$) between adjacent vortices in each layer, see Fig. 1.

A similar situation was considered in [1, 2], where the N-fold symmetric motion of $2N$ vortices in a two-dimensional (or barotropic) fluid was studied, and also in [32, 68], where a two-layer quasi-geostrophic model was used to study the special case of equal-radius N-gons in the two layers.

It is convenient to introduce the complex coordinate $z_j^\alpha = x_j^\alpha + iy_j^\alpha$ for the α^{th} vortex in layer j (with $j = 1$ in the top layer and $j = 2$ in the bottom one). The vortex strengths κ_j^α are set to $\kappa > 0$ in the bottom layer and $-\kappa$ in the top layer, corresponding to 'warm' hetons according to [31].

In an unbounded domain, the motion of the vortices in general is governed by the ordinary

differential equations (see [66])

$$\dot{\bar{z}}_j^\alpha = \frac{(-1)^j\kappa}{4\pi i}\Bigg\{\sum_{\substack{\beta=1\\ \beta\neq\alpha}}^{N}\frac{1}{z_j^\alpha - z_j^\beta}\Big[1+\gamma|z_j^\alpha - z_j^\beta|\mathrm{K}_1\Big(\gamma|z_j^\alpha - z_j^\beta|\Big)\Big] - \sum_{\beta=1}^{N}\frac{1}{z_j^\alpha - z_{3-j}^\beta}\Big[1-\gamma|z_j^\alpha - z_{3-j}^\beta|\mathrm{K}_1\Big(\gamma|z_j^\alpha - z_{3-j}^\beta|\Big)\Big]\Bigg\}, \tag{1}$$

where $j = 1, 2$ and $\alpha = 1, 2, \ldots, N$. Here, $\bar{}$ denotes complex conjugation, K_1 is the first-order modified Bessel function of the second kind, and $\gamma = 1/\lambda$ is inverse of the internal Rossby deformation length $\lambda = \sqrt{g'h_1h_2/(h_1+h_2)}/f$ with g' being the reduced gravity.

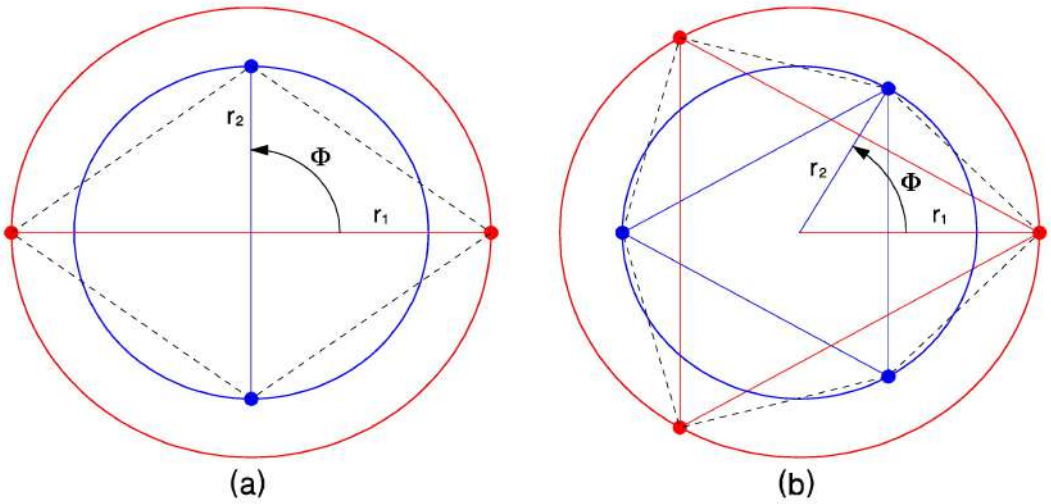

Figure 1: Schematic diagram of the initial vortex system with $r_2 < r_1$ (viewed from above): (a) $N = 2$ (the simplest case); (b) $N = 3$. The solid lines correspond to N-gons with circumscribed radii r_1 and r_2, and the dashed lines correspond to $2N$-gons (which joins the vortices of both N-gons). Red ('warm') / blue ('cold') colors correspond to top / bottom layers.

Eqs. (1) are invariant under both translation and rotation. It follows that the two real components, P_x and P_y, of the linear impulse and the angular impulse, M,

$$P_x + iP_y = \frac{\kappa}{2}\sum_{j=1}^{2}(-1)^j\sum_{\alpha=1}^{N}z_j^\alpha \qquad \text{and} \qquad M = \frac{\kappa}{2}\sum_{j=1}^{2}(-1)^j\sum_{\alpha=1}^{N}\Big|z_j^\alpha\Big|^2 \tag{2}$$

are constants of the motion. Moreover, the linear momentum is zero in each layer. The Hamiltonian, expressing energy conservation, takes the form

$$\mathcal{H} = -\frac{\kappa^2}{8\pi}\sum_{j=1}^{2}\Bigg\{\sum_{\substack{\alpha,\beta=1\\ \alpha\neq\beta}}^{N}\Big[\ln|z_j^\alpha - z_j^\beta| - \mathrm{K}_0\Big(\gamma|z_j^\alpha - z_j^\beta|\Big)\Big] - \sum_{\alpha,\,\beta=1}^{N}\Big[\ln|z_{(3-j)}^\alpha - z_j^\beta| + \mathrm{K}_0\Big(\gamma|z_{(3-j)}^\alpha - z_j^\beta|\Big)\Big]\Bigg\}, \tag{3}$$

where K_0 is the zeroth-order modified Bessel function of the second kind.

2 Symmetry reduction

We now restrict attention to the N-fold symmetric situation. It follows from the invariants Eq. (2) that this symmetry is preserved for all time. Moreover, one can to find a solution of Eqs. (1) of the form

$$z_j^\alpha = z_j(t)e^{i\frac{2\pi(\alpha-1)}{N}} = r_j(t)e^{i\left(\varphi_j(t)+\frac{2\pi(\alpha-1)}{N}\right)}. \tag{4}$$

For the initial configuration described in Fig. 1, the initial angles are $\varphi_1(0) = 0$, $\varphi_2(0) = \pi/N$. Substituting a solution of the form Eq. (4) into Eqs. (1) allows one to obtain (after some algebra) the equations for the radial and angular coordinates of an equivalent heton. This heton consists of one vortex in the top layer and one vortex in the bottom layer. The coordinates satisfy the ordinary differential equations

$$\begin{aligned}\dot{r}_j &= \frac{(-1)^j\kappa}{4\pi r_j}\Bigg[\gamma r_j\sum_{n=0}^{N-1}\frac{\varrho^{(3-2j)}\sin\left(\Phi+\frac{2\pi n}{N}\right)}{G_j\left(\varrho,\Phi,n\right)}\mathrm{K}_1(\gamma r_j G_j(\varrho,\Phi,n)) \\ &- \frac{N\varrho^{N(3-2j)}\sin N\Phi}{1+\varrho^{N(3-2j)}\left(\varrho^{N(3-2j)}-2\cos N\Phi\right)}\Bigg],\end{aligned} \tag{5}$$

and

$$\begin{aligned}\dot{\varphi}_j &= \frac{(-1)^j\kappa}{4\pi r_j^2}\Bigg[\gamma r_j\sum_{n=1}^{N-1}\sin\frac{\pi n}{N}\mathrm{K}_1\left(2\gamma r_j\sin\frac{\pi n}{N}\right) \\ &+ \gamma r_j\sum_{n=0}^{N-1}\frac{1-\varrho^{(3-2j)}\cos\left(\Phi+\frac{2\pi n}{N}\right)}{G_j\left(\varrho,\Phi,n\right)}\mathrm{K}_1\left(\gamma r_j G_j\left(\varrho,\Phi,n\right)\right) \\ &+ \frac{N-1}{2}-\frac{N\left(1-\varrho^{N(3-2j)}\cos N\Phi\right)}{1+\varrho^{N(3-2j)}\left(\varrho^{N(3-2j)}-2\cos N\Phi\right)}\Bigg]\end{aligned} \tag{6}$$

for $j = 1$ and 2. In the above, $\varrho \equiv r_2/r_1$, $\Phi \equiv \varphi_2 - \varphi_1$ and

$$G_j(\varrho,\,\Phi,\,n) = \sqrt{1+\varrho^{(3-2j)}\left[\varrho^{(3-2j)}-2\cos\left((-1)^{j-1}\Phi+\frac{2\pi n}{N}\right)\right]},$$

where $n = 0,\, 1,\, \ldots,\, N-1$.

To derive Eqs. (5)-(6), we have used

$$\sum_{n=1}^{N-1}\frac{1}{1-e^{i\frac{2\pi n}{N}}} = \frac{N-1}{2}, \qquad \sum_{n=0}^{N-1}\frac{1}{1-\varrho^{(3-2j)}e^{i\frac{2\pi n}{N}}} = \frac{N}{1-\varrho^{N(3-2j)}}$$

and the straightforward equality

$$\sum_{n=1}^{N-1}\frac{\sin\frac{\pi n}{N}\sin\frac{2\pi n}{N}}{1-\cos\frac{2\pi n}{N}}\mathrm{K}_1\left(2\gamma r_j\sin\frac{\pi n}{N}\right) = 0.$$

This is zero because for N even, the terms in the sum cancel pairwise. For N odd, the unpaired term in the sum is zero. In this way, we have reduced the original system of $4N$ Eqs. (1) to a system of just 4 equations, Eqs. (5) and (6). The trajectories of the remaining $N-1$ hetons differ from those obtained from Eqs. (5) and (6) simply by a rotation through $2\pi n/N$.

3 The equations of motion of a 'virtual' vortex

For a general qualitative analysis of this reduced dynamical system, it is convenient to further reduce Eqs. (5) – (6) to a system of two equations for a certain 'virtual' vortex.

The expression Eq. (2) for the angular momentum M allows one to eliminate one of the radial coordinates, for example

$$r_2 = \sqrt{|2\tilde{M}/N + (r_1)^2|},$$

where $\tilde{M} = M/\kappa$. Moreover, the right-hand sides of Eqs. (5) – (6) depend only on Φ, the angular difference between the lower and upper-layer vortices having the same index j. This allows us to form just two equations for $\varrho = r_2/r_1$ and $\Phi = \varphi_2 - \varphi_1$:

$$\begin{aligned}\dot{\varrho} &= -\frac{\kappa(1-\varrho^2)}{4\pi\varrho R^2}\Bigg[\sum_{n=0}^{N-1}\frac{\gamma R\varrho\sin(\Phi+\frac{2\pi n}{N})}{G_1(\varrho,\Phi,n)}\mathrm{K}_1\Big(\gamma R G_1(\varrho,\Phi,n)\Big) \\ &- \frac{N\varrho^N\sin N\Phi}{1+\varrho^N(\varrho^N-2\cos N\Phi)}\Bigg] \qquad (7)\end{aligned}$$

and

$$\begin{aligned}\dot{\Phi} &= \frac{\kappa}{4\pi R^2}\sum_{j=1}^{2}\varrho^{2(1-j)}\Bigg[\sum_{n=1}^{N-1}A_n^j + \sum_{n=0}^{N-1}\frac{\gamma R\varrho^{j-1}C_n^j}{G_j(\varrho,\Phi,n)}\mathrm{K}_1\Big(\gamma R\varrho^{j-1}G_j(\varrho,\Phi,n)\Big) \\ &+ \frac{N-1}{2} - \frac{N(1-\varrho^{N(3-2j)}\cos N\Phi)}{1+\varrho^{N(3-2j)}(\varrho^{N(3-2j)}-2\cos N\Phi)}\Bigg]. \qquad (8)\end{aligned}$$

Above, $R = r_1 = \sqrt{\frac{2}{N}\frac{\tilde{M}}{\varrho^2-1}}$, while

$$\begin{aligned}A_n^j &= \gamma R\varrho^{j-1}\sin\frac{\pi n}{N}\mathrm{K}_1\Big(2\gamma R\varrho^{j-1}\sin\frac{\pi n}{N}\Big), \\ C_n^j &= 1-\varrho^{3-2j}\cos\Big((-1)^{j-1}\Phi+\frac{2\pi n}{N}\Big).\end{aligned}$$

The last term in Eq. (7) vanishes for $\Phi = \frac{m\pi}{N}$. Furthermore, a rotation of the vortices in either layer through an angle of $\frac{2\pi}{N}$ does not change the state of the system, so it suffices to consider only the values $\Phi = 0$ and $\Phi = \frac{\pi}{N}$. In both cases, the equalities $(\dots)_i = -(\dots)_{N-i}$ hold, where $(\dots)$ are the expressions within the sums. It follows that the right-hand side of (7) vanishes for these values of Φ, and ϱ reaches an extremum. It means

$$\dot{\varrho}\Big(\Phi = 0, \quad \frac{\pi}{N}\Big) = 0. \qquad (9)$$

The same is true for $r_{1,2}$ since

$$\dot{r}_1 = \dot{R} = \frac{R\varrho}{1-\varrho^2}\dot{\varrho}, \qquad \dot{r}_2 = \dot{\varrho}R + \varrho\dot{R}. \qquad (10)$$

Also, from Eq. (8), one can see that $\dot{\Phi}(\Phi = 0)$ does not change sign as a function of ϱ.

The Hamiltonian Eq. (3) in the variables (R, Φ) takes the form

$$\begin{aligned}\mathcal{H} = &-\frac{\kappa^2}{4\pi}\sum_{j=1}^{2}\Bigg[\sum_{n=1}^{N-1}\Bigg(\ln\Big(2R\varrho^{j-1}\sin\frac{\pi n}{N}\Big) - \mathrm{K}_0\Big(2\gamma R\varrho^{j-1}\sin\frac{\pi n}{N}\Big)\Bigg) \\ &- \sum_{n=0}^{N-1}\Bigg(\ln\Big(R\varrho^{j-1}G_j(\varrho,\Phi,n)\Big) + \mathrm{K}_0\Big(\gamma R\varrho^{j-1}G_j(\varrho,\Phi,n)\Big)\Bigg)\Bigg]. \qquad (11)\end{aligned}$$

This will prove useful for constructing phase portraits of the dynamics.

4 Analysis of possible motion regimes for $N = 2$

We next specialise to $N = 2$, i.e. two vortices per layer. In this case the Hamiltonian becomes

$$\begin{aligned}\frac{4\pi\mathcal{H}}{-\kappa^2} &= \ln\left(\frac{4\varrho}{R^2\big(1+\varrho^2\,(\varrho^2-2\cos 2\Phi)\big)}\right) - \mathrm{K}_0(2\gamma R) - \mathrm{K}_0(2\gamma R\varrho) \\ &- 2\mathrm{K}_0\big(\gamma R\sqrt{1+\varrho(\varrho-2\cos\Phi)}\big) - 2\mathrm{K}_0\big(\gamma R\sqrt{1+\varrho\,(\varrho+2\cos\Phi)}\big). \end{aligned} \tag{12}$$

As in [37, 54], we analyse the form of the Hamiltonian at the extrema in ϱ, where $\Phi = \pi/2$ or 0. There, respectively, we have

$$\begin{aligned}\frac{4\pi\mathcal{H}\left(\Phi=\frac{\pi}{2}\right)}{-\kappa^2} \equiv \frac{4\pi\mathcal{H}^+}{-\kappa^2} &= \ln\left(\frac{4\varrho}{R^2(1+\varrho^2)^2}\right) - \mathrm{K}_0(2\gamma R) - \mathrm{K}_0(2\gamma R\varrho) \\ &- 4\mathrm{K}_0(\gamma R\sqrt{1+\varrho^2}), \\ \frac{4\pi\mathcal{H}\left(\Phi=0\right)}{-\kappa^2} \equiv \frac{4\pi\mathcal{H}^-}{-\kappa^2} &= \ln\left(\frac{4\varrho}{R^2(1-\varrho^2)^2}\right) - \mathrm{K}_0(2\gamma R) - \mathrm{K}_0(2\gamma R\varrho) \\ &- 2\mathrm{K}_0\big(\gamma R(1-\varrho)\big) - 2\mathrm{K}_0\big(\gamma R(1+\varrho)\big). \end{aligned} \tag{13}$$

We next study the dependence of these functions on ϱ. We consider only the interval $0 < \varrho < 1$, since the situation $\varrho > 1$ corresponds to exchanging the two layers. In other words, we may consider $0 < \varrho < 1$ without loss of generality.

One can see that as $\varrho \to 0$, both extreme values of the Hamiltonian tend to infinity. However, $\mathcal{H}^+ = \mathcal{H}(\Phi = \pi/2)$ also tends to infinity as $\varrho \to 1$, whereas $\mathcal{H}^- = \mathcal{H}(\Phi = 0)$ is bounded by the finite value of $2\ln\gamma$.

For general Φ, and for $N = 2$, Eqs. (7)–(8) for the virtual vortex become

$$\begin{aligned}\dot{\varrho} &= -\frac{\kappa(1-\varrho^2)\sin\Phi}{4\pi R^2}\Bigg[\gamma R\Bigg(\frac{\mathrm{K}_1\left(\gamma R\sqrt{1+\varrho\,(\varrho-2\cos\Phi)}\right)}{\sqrt{1+\varrho\,(\varrho-2\cos\Phi)}} \\ &- \frac{\mathrm{K}_1\left(\gamma R\sqrt{1+\varrho\,(\varrho+2\cos\Phi)}\right)}{\sqrt{1+\varrho\,(\varrho+2\cos\Phi)}}\Bigg) - \frac{4\varrho\cos\Phi}{1+\varrho^2(\varrho^2-2\cos 2\Phi)}\Bigg] \end{aligned} \tag{14}$$

and

$$\begin{aligned}\dot{\Phi} &= \frac{\gamma\kappa}{4\pi R}\Bigg[\mathrm{K}_1(2\gamma R) + \frac{\mathrm{K}_1(2\gamma R\varrho)}{\varrho} + \Big(2-\big(\varrho+\varrho^{-1}\big)\cos\Phi\Big)\frac{\mathrm{K}_1\left(\gamma R\sqrt{1+\varrho\,(\varrho-2\cos\Phi)}\right)}{\sqrt{1+\varrho\,(\varrho-2\cos\Phi)}} \\ &+ \Big(2+\big(\varrho+\varrho^{-1}\big)\cos\Phi\Big)\frac{\mathrm{K}_1\left(\gamma R\sqrt{1+\varrho\Big(\varrho+2\cos\Phi\Big)}\right)}{\sqrt{1+\varrho\,(\varrho+2\cos\Phi)}} \\ &+ \frac{1}{\gamma R}\frac{1+\varrho^2}{2\varrho^2}\Big(1-\frac{4\varrho^2(1-\cos 2\Phi)}{1+\varrho^2(\varrho^2-2\cos 2\Phi)}\Big)\Bigg]. \end{aligned} \tag{15}$$

These are next used to show that $\mathcal{H}^-$ is a monotonically decreasing function of ϱ. We start from the fact that the angular velocity $\dot{\Phi}$ is proportional to the derivative of the Hamiltonian with respect to ϱ. Applying Eq. (15) at $\Phi = 0$, we find

$$\begin{aligned}\dot{\Phi}\,(\Phi=0) \equiv \dot{\Phi}^- &= \frac{\gamma\kappa}{4\pi R}\Bigg[\mathrm{K}_1(2\gamma R) + \frac{\mathrm{K}_1(2\gamma R\varrho)}{\varrho} + \frac{(1-\varrho)}{\varrho}\mathrm{K}_1\Big(\gamma R\,(1-\varrho)\Big) \\ &+ \frac{(1+\varrho)}{\varrho}\mathrm{K}_1\Big(\gamma R\,(1+\varrho)\Big) + \frac{1}{\gamma R}\frac{1+\varrho^2}{2\varrho^2}\Bigg], \end{aligned} \tag{16}$$

showing that this does not change sign but monotonously decreases as ϱ increases. It follows that $\mathcal{H}^-$ is monotonically decreasing. This is true in fact for arbitrary N.

Notably, the second time derivative of ϱ for $\Phi = 0$ is always negative,

$$\ddot{\varrho}\left(\Phi=0\right) = -\frac{\left(1-\varrho^2\right)}{4\pi R^2}\dot{\Phi}\left[\gamma R\left(\frac{\mathrm{K}_1\left(\gamma R\left(1-\varrho\right)\right)}{\left(1-\varrho\right)} - \frac{\mathrm{K}_1\left(\gamma R\left(1+\varrho\right)\right)}{\left(1+\varrho\right)}\right) - \frac{4\varrho}{\left(1-\varrho^2\right)^2}\right] < 0, \quad (17)$$

showing that this extremum is always a minimum.

The situation with $\mathcal{H}^+$ is different. The corresponding angular velocity takes the form

$$\begin{aligned}\dot{\Phi}\left(\Phi=\frac{\pi}{2}\right) \equiv \dot{\Phi}^+ &= \frac{\gamma\kappa}{4\pi R}\left[\mathrm{K}_1(2\gamma R) + \frac{\mathrm{K}_1(2\gamma R\varrho)}{\varrho} + 4\frac{\mathrm{K}_1\left(\gamma R\sqrt{1+\varrho^2}\right)}{\sqrt{1+\varrho^2}}\right. \\ &+ \left.\frac{1}{\gamma R}\frac{1}{2\varrho^2}\left(\frac{\left(1+\varrho^2\right)^2 - 8\varrho^2}{\left(1+\varrho^2\right)}\right)\right] \end{aligned} \quad (18)$$

and obviously can change sign. Thus $\mathcal{H}^+(\varrho)$ has a minimum.

We also note that these Hamiltonian curves do not intersect, since their difference

$$\begin{aligned}\frac{4\pi\left(\mathcal{H}^+ - \mathcal{H}^-\right)}{-\kappa^2} &= \ln\left(\frac{\left(1-\varrho^2\right)^2}{\left(1+\varrho^2\right)^2}\right) - 4\mathrm{K}_0\left(\gamma R\sqrt{1+\varrho^2}\right) + 2\mathrm{K}_0\Big(\gamma R(1-\varrho)\Big) \\ &+ 2\mathrm{K}_0\Big(\gamma R(1+\varrho)\Big) \end{aligned} \quad (19)$$

is always positive on the interval $0 < \varrho < 1$.

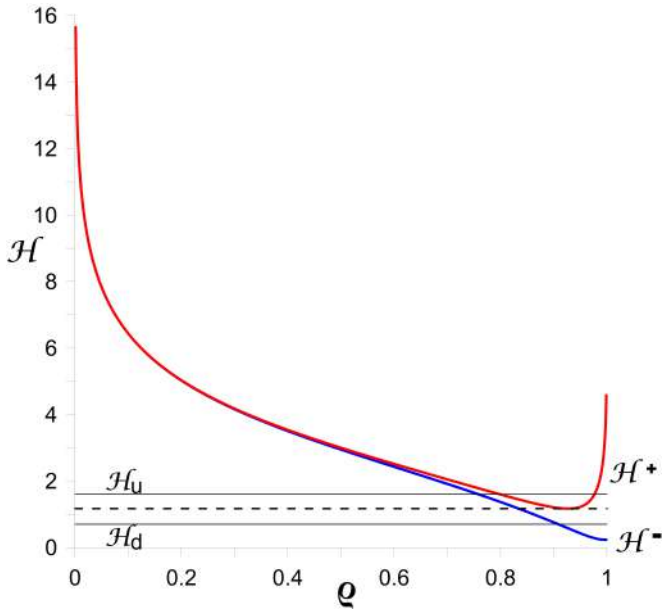

Figure 2: Extremal Hamiltonian curves $\mathcal{H}^+(\varrho)$ (red line) and $\mathcal{H}^-(\varrho)$ (blue line) as a function of ϱ at $\tilde{M} = -0.5$. The dashed horizontal line shows the minimum value of $\mathcal{H}^+$, denoted $\mathcal{H}^{+*}$, found at $\varrho = \varrho^*$ (here at approximately $\varrho^* = 0.95$). Two additional lines of constant energy are drawn in solid: $\mathcal{H} = \mathcal{H}_\mathrm{u}$ lying above $\mathcal{H}^{+*}$, and $\mathcal{H} = \mathcal{H}_\mathrm{d}$ lying below $\mathcal{H}^{+*}$. The intersection of either line with $\mathcal{H}^-(\varrho)$ is denoted by ϱ^-. Note, the line $\mathcal{H} = \mathcal{H}_\mathrm{u}$ intersects the curve $\mathcal{H}^+$ at two points, which we denote $\varrho = \varrho^{+1}$ and ϱ^{+2}, with $\varrho^{+2} > \varrho^{+1}$.

We next examine the possible localized (e.g. periodic) and non-localized (e.g. diverging) types of motion. For this, it is convenient to introduce the following definitions, which are

depicted graphically in Fig. 2. Let ϱ^* be the value of ϱ for which the function $\mathcal{H}^+$ has a minimum $\mathcal{H}^{+*}$ (the dashed horizontal line in the figure). Let ϱ^- be the intersection point between $\mathcal{H}^-(\varrho)$ and either of two levels of constant energy, $\mathcal{H} = \mathcal{H}_\mathrm{d}$ or $\mathcal{H}_\mathrm{u}$, defined so that $\mathcal{H}_\mathrm{d} < \mathcal{H}^{+*}$ and $\mathcal{H}_\mathrm{u} > \mathcal{H}^{+*}$. Finally, let ϱ^{+1} and ϱ^{+2} be the minimum and the maximum solutions of $\mathcal{H}^+(\varrho) = \mathcal{H}_\mathrm{u}$.

From Fig. 2, one can deduce three possible regimes of motion of the virtual vortex:

(A) Unbounded motion occurring within the interval $\varrho^- \leq \varrho \leq 1$, when $\mathcal{H} < \mathcal{H}^{+*}$.

(B) Localized (bounded) motion occurring within the interval $\varrho^- \leq \varrho \leq \varrho^{+1}$, when $\mathcal{H} > \mathcal{H}^{+*}$.

(C) Unbounded motion occurring within the interval $\varrho^{+2} \leq \varrho \leq 1$, when $\mathcal{H} > \mathcal{H}^{+*}$.

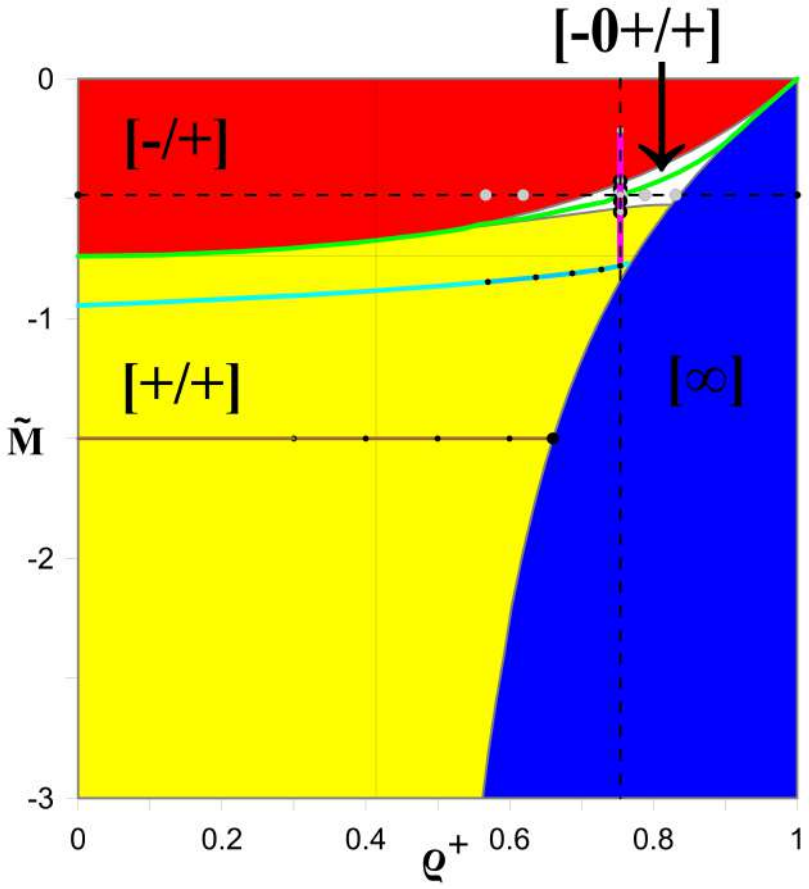

Figure 3: Regime diagram showing the possible types of motion in plane spanned by ϱ^+ and $\tilde{M}$, for the initial value $\Phi_0 = \pi/2$. The blue $[\infty]$ region corresponds to unbounded motion, while the red $[-/+]$, white $[-0+/+]$ and yellow $[+/+]$ regions correspond to localized, bounded motions in which all vortices in both layers move within annular zones between concentric circles (see text for details). The thin vertical line at $\varrho^+ \sim 0.414$ is the asymptote for $\tilde{M} \to -\infty$, while the thin horizontal line $\tilde{M} \sim -0.7398$ divides the regions $[-/+]$ and $[+/+]$ at $\varrho^+ = 0$. Furthermore, the $[-\mathbf{0}+/+]$ region thins as $\varrho^+ \to 0$ and vanishes at $\varrho^+ = 0$ and $\tilde{M} \sim -0.7398$. The markers show the locations of the numerical simulations presented below in Figs. 4 and 7-16. When constructing this Figure and Figures 7-16, we have taken $\gamma = 1$.

Thus, if we initialise the system with $\varrho(0) = \varrho_0 = \varrho^+$ and $\Phi(0) = \Phi_0 = \pi/2$, and choose a value of the angular momentum $\tilde{M}$ to determine the initial values of the radial coordinates r_{10} and r_{20}, the subsequent motion will be localized (bounded) if $\varrho^+ < \varrho^*$, but unbounded if $\varrho^+ > \varrho^*$, see Fig. 3. Both cases in fact correspond to the same condition: $\mathcal{H} > \mathcal{H}^{+*}$. It is worth mentioning that it is impossible to have $\mathcal{H} < \mathcal{H}^{+*}$ for the specified initial condition $\varrho(0) = \varrho_0 = \varrho^+$ and $\Phi(0) = \Phi_0 = \pi/2$, irrespective of $\tilde{M}$. We consider $\mathcal{H} < \mathcal{H}^{+*}$ separately below.

The region of unbounded motions $[\infty]$ is shaded in blue in Fig. 3. The critical curve $\tilde{M}(\varrho^*)$ separating bounded and unbounded motion in parameter space is found in practice by setting the right-hand side of (18) to zero, for each value of $\tilde{M}$, and solving the resulting equation for ϱ. Notably, it is possible to determine the asymptotic form of this critical curve for both small and large values of $-\tilde{M}$. Eq. (18) has no solutions for $-\tilde{M} \gg 1$ and $\varrho \ll 1$, so we can assume that $\varrho R \gg 1$. It follows that the modified Bessel functions in equation Eq. (18) are exponentially small, and hence that the critical curve $\tilde{M}(\varrho^*)$ tends to

$$\lim_{\tilde{M}\to-\infty} \varrho = \sqrt{2} - 1. \tag{20}$$

This asymptote is shown in Fig. 3 by a vertical line (the edge of the $[\infty]$ region approaches it when $-M \to \infty$). Also, there are no solutions when $-\tilde{M} \ll 1$ and $\varrho R \ll 1$. This means that, for small $-\tilde{M}$, the condition $\varrho \to 1$ holds, corresponding to the limit of equal radii, $r_1 \to r_2$. Then Eq. (18) reduces to

$$\mathrm{K}_1(2\gamma R) + \sqrt{2}\mathrm{K}_1\left(\gamma R\sqrt{2}\right) - \frac{1}{2\gamma R} = 0, \tag{21}$$

whose solution is $\gamma R = \lim_{\varrho\to 1} \gamma\sqrt{-\tilde{M}/(1-\varrho^2)} = 1.127597$. Hence the edge of the $[\infty]$ region tends to the point $(\tilde{M}, \varrho) = (0, 1)$ along the curve

$$\tilde{M} = \frac{1.271475}{\gamma^2}\left(\rho^2 - 1\right). \tag{22}$$

If $\varrho = 1$ at $t = 0$, it follows from (14) that $\varrho = 1$ for all times since $\dot{\varrho} = 0$ identically. For this special case, Eq. (15) simplifies to

$$\begin{aligned}\dot{\Phi} = \frac{\kappa}{4\pi R^2}\Big[2\gamma R\mathrm{K}_1(2\gamma R) \;&+\; \gamma R\sqrt{2(1-\cos\Phi)}\mathrm{K}_1\Big(\sqrt{2(1-\cos\Phi)}\Big) \\ &+\; \gamma R\sqrt{2(1+\cos\Phi)}\mathrm{K}_1\Big(\sqrt{2(1+\cos\Phi)}\Big) - 1\Big],\end{aligned} \tag{23}$$

where $R = r_1 = r_2$.

Hogg and Stommel in [31] showed (see also [34,66,68]) that for $R \leq 0.717$ the solutions to Eq. (23) are localized and periodic, and moreover the corresponding trajectories follow closed quasi-quadrangular patterns. For $R > 0.717$, the trajectories are unbounded. As $R \to \infty$ we have $\dot{\Phi} \sim \kappa/(2\pi R^2) \to 0$, i.e. $\Phi \sim const$, and, due to the axial symmetry, $\Phi \sim \pi/2$.

4.1 Direction of rotation of the external vortices

Let us next consider the characteristics of the localized, bounded vortex motions. Below, we show that the internal vortices (located closer to each other) never change the direction of their cyclonic motion about their centre. The direction of the motion of the external vortices however varies, depending on the region of the parameter space. The external vortices are

expected to rotate in the opposite (anticyclonic) direction if the interaction between the vortices in the two layers is sufficiently weak. In the parameter space $(\varrho^+; \tilde{M})$ in Fig. 3, this counter-rotating motion occurs in the red $[-/+]$ region.

To determine the edge of this region, we write the equation of the curve $\tilde{M}(\varrho^+)$ along which the angular velocity of the external vortices (i.e. the vortices in the upper layer) vanishes:

$$\dot{\varphi}_1^+ = \frac{-\kappa}{4\pi R^2}\left[\gamma R \mathrm{K}_1(2\gamma R) + 2\gamma R \frac{\mathrm{K}_1\left(\gamma R\sqrt{1+\varrho^2}\right)}{\sqrt{1+\varrho^2}} + \frac{\varrho^2-3}{2(1+\varrho^2)}\right] = 0. \tag{24}$$

Solving this nonlinear equation provides $\tilde{M}(\varrho^+)$. Analytical progress can be made assuming $\varrho \ll 1$; then Eq. (24) reduces to

$$\dot{\varphi}_1^+ = \frac{-\kappa}{4\pi R^2}\left[\gamma R \mathrm{K}_1(2\gamma R) + 2\gamma R \mathrm{K}_1(\gamma R) - \frac{3}{2}\right] = 0, \tag{25}$$

whose solution is

$$\gamma R = \gamma\sqrt{\frac{-\tilde{M}}{1-\varrho^2}} \approx 0.8602. \tag{26}$$

Thus the edge of the $[-/+]$ region tends to $\tilde{M} \approx -0.7398/\gamma^2$ when $\varrho \to 0$. Also, one can show that when $\varrho \to 1$, the edge of this region as well as that of $[\infty]$ asymptote the line $\tilde{M} = R(1-\varrho)$ (not shown).

Let us next consider the direction of rotation of the internal vortices (i.e. the vortices in the lower layer).[1] Their angular velocity at the minimum of r_2 (when $\Phi = 0$, see Eqs. (9) and (10)) is found from

$$\dot{\varphi}_2^- = \frac{\kappa}{4\pi R^2}\left[\frac{\gamma R}{\varrho}\Big(\mathrm{K}_1(2\gamma R) + \mathrm{K}_1\big(\gamma R(1-\varrho)\big) + \mathrm{K}_1\big(\gamma R(1+\varrho)\big)\Big) + \frac{1}{2} + \frac{2\varrho^2}{1-\varrho^2}\right]. \tag{27}$$

This is always positive, implying that the internal vortices never change their direction of rotation at this distance. At the maximum of r_2, the value of $\dot{\Phi}^+$ vanishes only at the edge of the blue $[\infty]$ region. It follows that $\dot{\varphi}_2^+$ must be opposite in sign to $\dot{\varphi}_1^+$ at this distance, i.e. it is also positive at the maximum distance. This confirms that the internal vortices always rotate in the same direction.

We next analyse the edge of the yellow $[+/+]$ region shown in Fig. 3, where the vortices in the two layers rotate in the same direction. At this edge (the curve $\tilde{M}(\varrho^+)$), the angular velocity of the external vortices vanishes at the minimum of r_1. It thus cannot change sign at any value of r_1. The equation for the curve $\tilde{M}(\varrho^+)$ is

$$\dot{\varphi}_1^- = \frac{-\kappa}{4\pi R^2}\left[\gamma R\Big(\mathrm{K}_1(2\gamma R) + \mathrm{K}_1\big(\gamma R(1-\varrho)\big) + \mathrm{K}_1\big(\gamma R(1+\varrho)\big)\Big) + \frac{1}{2} - \frac{2}{1-\varrho^2}\right]. \tag{28}$$

This curve coincides with the edge of the red $[-/+]$ region shown in Fig. 3, in the limit $\varrho \ll 1$, and reaches the same limiting point given in Eq. (26).

There are no solutions for $\varrho \to 1$, even if we allow $\tilde{M} \to -\infty$. It follows that the edges of the yellow $[+/+]$ and blue $[\infty]$ regions intersect at a finite value of ϱ and $\tilde{M}$, as has been confirmed numerically.

[1] Here and everywhere below we will use the terms 'internal vortex' and 'lower-layer vortex' as synonyms, as well as 'external vortex' and 'upper-layer vortex'.

There is a small region between the $[-/+]$ and $[+/+]$ regions, shown in white in Fig. 3, where angular velocity of the external vortices changes sign over the period T_2 of oscillation. The green curve lying inside this region indicates where the *time-averaged* angular velocity, $\langle\dot{\varphi}_1\rangle_{T_2}$, vanishes. Along this curve, the external vortices only nutate, with no net rotation over a period.

In what follows, we denote the ratio of the periods of oscillation of the internal and external vortices by $\delta = T_2/T_1$. This parameter helps to delineate the various forms of motion which may occur.

4.2 Examples of localized trajectories: complex absolute choreographies

We next present examples of the vortex motion. In all cases, we show a top view of the trajectories of the equivalent heton (one vortex in each layer). The negative upper-layer vortex, initially at $(r, \varphi) = (r_{10}, 0)$, is shown in red, while the positive lower-layer vortex, initially at $(r, \varphi) = (r_{20}, \pi/2)$, is shown in blue. In Fig. 1(a) these vortices correspond to the right and top vortices, respectively. These initial conditions imply $\Phi_0 = \pi/2$ for the virtual vortex.

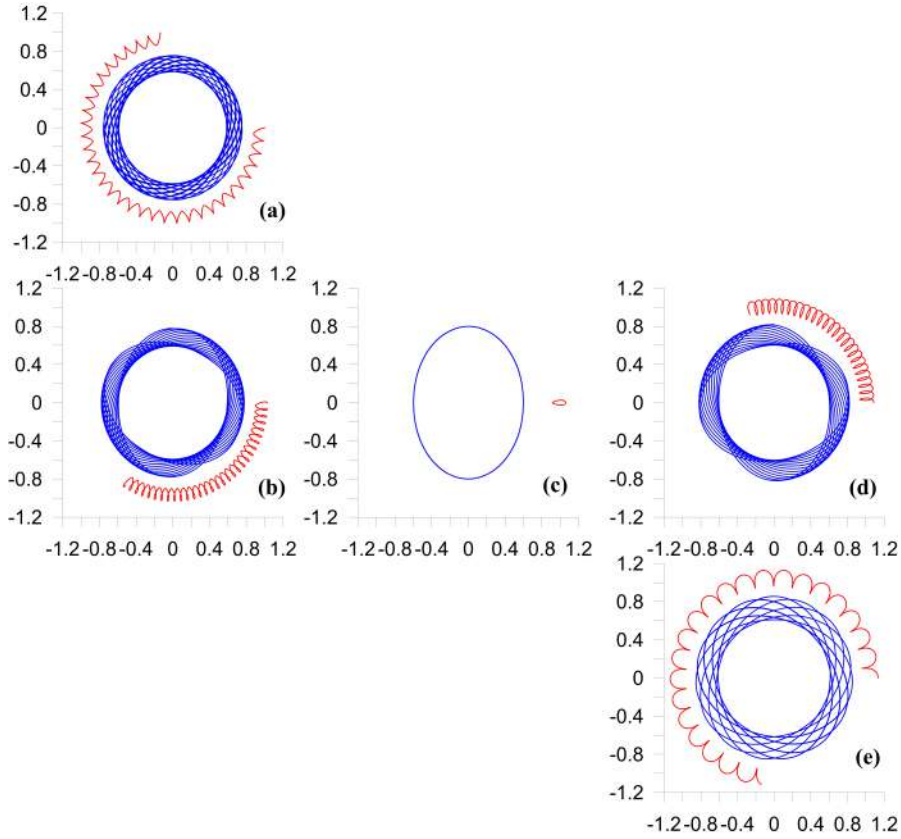

Figure 4: Examples of vortex trajectories for the equivalent heton. As in Fig. 1, the red/blue colour corresponds to the upper/lower layer. The initial states for these five simulations correspond to 5 round black markers in the vertical segment at $\varrho^+ = 0.754$ and $\tilde{M}$ = -0.425, -0.460, -0.485, -0.510 & -0.555 in Fig. 3. Panels (a) and (e) show examples in the regimes $[-/+]$ and $[+/+]$ (red and yellow areas of the diagram), respectively. Panels (b), (c) and (d) show three examples of trajectories in the regime $[-\mathbf{0}+/+]$ (white area of the diagram).

Fig. 4 shows examples of vortex trajectories in three different regimes. The initial condi-

tions all take $\varrho^+ = 0.754$ but have different values of angular momentum $\tilde{M}$ (marked by the black closed circles in Fig. 3). The case $\tilde{M} = -0.425$ belongs to the $[-/+]$ region, and the corresponding trajectory is shown in panel (a) of Fig. 4. Here we see the anticyclonic motion of the upper-layer vortex, whose trajectory displays externally pointing cycloidal cusps. The case $\tilde{M} = -0.555$ belongs to the $[+/+]$ region in which the upper-layer vortex moves cyclonically. This case is shown in panel (e). Here the trajectory of the upper-layer vortex is also cycloidal, but with inward pointing cusps. The three intermediate angular momentum cases in Fig. 3 belong to the $[-\mathbf{0}+/+]$ region of the diagram. From top to bottom (i.e. in order of decreasing $\tilde{M}$), they are shown in panels (b), (c) and (d), respectively. The special case shown in (c), for $\tilde{M} = -0.485$, corresponds to the critical case where the external vortices only nutate, i.e. with no net rotation (subregime $[\mathbf{0}/+]$ in the present notation). Lower (more negative) $\tilde{M}$ leads to cyclonic rotation as in (d), while higher $\tilde{M}$ leads to anti-cyclonic rotation as in (b). The qualitative difference between panels (b)–(d) and panels (a) & (e) is the loop-like (as opposed to cycloidal) trajectories of the upper-layer vortex. This is due to the periodically-alternating direction of rotation of the external vortices, and is unique to the $[-\mathbf{0}+/+]$ region.

We next examine in more detail the periodic motion occurring for initial conditions lying on the green curve inside the white $[-\mathbf{0}+/+]$ region. An example of the trajectories of the equivalent heton was already shown in panel (c) of Fig. 4. Recall that Fig. 4 only shows the trajectories of one of the two hetons. The other is found on the opposite side of the origin. Thus, the two vortices in the lower layer rotate in a cyclonic direction along a common trajectory at opposite ends of this quasi-elliptic curve. This is an example of *complex absolute choreography*.[2] The two vortices in the upper layer perform a nutation around a common centre with an alternating angular velocity. The rotation periods T_1 and T_2 of the upper and lower-layer vortices are commensurate: they have a ratio 1 : 2, i.e. $\delta = T_2/T_1 = 2$. The upper-layer vortices either rotate around stationary peripheral points, or exhibit closed figure of 8 trajectories (see next section).

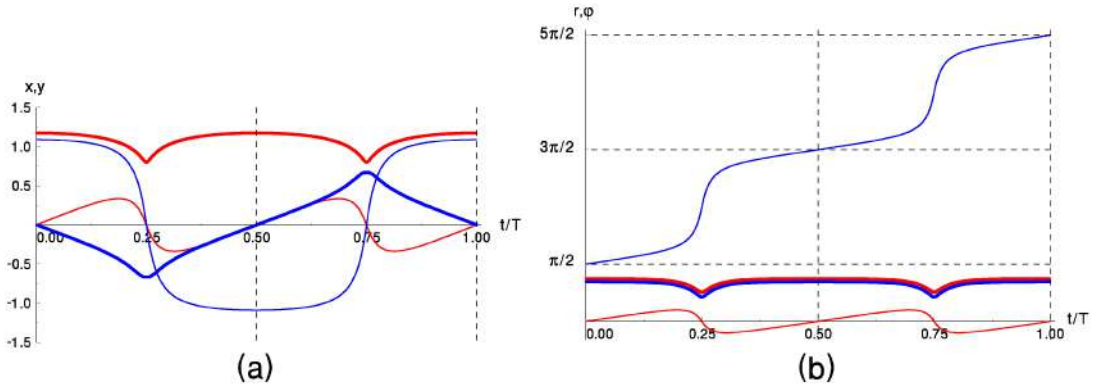

Figure 5: Time evolution of the (a) Cartesian coordinates (x thick, y thin) and (b) polar coordinates (r thick, φ thin) of the equivalent heton, solving (5) - (6) over the interval $[0; T_2]$ for a periodic solution having $\varrho^+ = 0.754$ and $\tilde{M} = -0.485$. The upper/lower-layer vortex is shown in red/blue.

This is shown in Fig. 5 for the interval $[0; T_2]$, clearly corresponding to two periods of the

[2]In 2001, Simó [59] introduced the concept of *choreography*. Choreographies can be (a) *absolute* if the trajectories are closed in a fixed coordinate system; (b) *relative* if the trajectories are closed in a uniformly rotating or translating coordinate system; (c) *simple* if all of the vortices move along a common trajectory; and (d) *complex* if at least one of the vortices moves along a separate trajectory.

upper-layer vortex's motion. The lower-layer vortex makes one full revolution from $\varphi = \pi/2$ to $5\pi/2$, while the upper-layer vortex returns to its original position twice. For this class of periodic motions, it is noteworthy that: (1) the functions $r_1(t)$ and $r_2(t)$ behave in a similar way, reaching extreme values simultaneously (this property is due to angular momentum conservation and is observed for all finite vortex motions); and (2) the speed of the vortices is not uniform — they slow down in the vicinity of the maximum values of $r_1(t)$ and $r_2(t)$ and accelerate near their minimum values.

4.3 Analysis of the periods of oscillation and rotation

There are two characteristic periods in the vortex motion: (1) T_0 – the time it takes a vortex to move from its maximum radius to its minimum radius and back, and (2) T_r – the time it takes a vortex to rotate around the origin, i.e. through an angular difference of 2π. Let us consider the ratio of these periods

$$\frac{\langle\dot{\Phi}\rangle_{T_0}}{\langle\dot{\varphi}_1\rangle_{T_r}} = \frac{\langle\dot{\varphi}_2 - \dot{\varphi}_1\rangle_{T_0}}{\langle\dot{\varphi}_1\rangle_{T_r}} = \frac{\langle\dot{\varphi}_2\rangle_{T_0}}{\langle\dot{\varphi}_1\rangle_{T_r}} - 1 = \frac{T_r}{T_0} \equiv \delta_{max}. \tag{29}$$

First of all, on the green curve in Fig. 3, we know that $\langle\dot{\varphi}_1\rangle_{T_r} = 0$ since only nutation occurs in this layer, whereas $\langle\dot{\varphi}_2\rangle_{T_0}$ has a positive finite value. Therefore, $\delta_{max} \to \infty$ on this curve. On the other hand, $\delta_{max} \to 0$ on the edge of the $[\infty]$ region of unbounded motions. Indeed, on this edge $\dot{\varrho} = \dot{\Phi} = 0$ for $\Phi = \pi/2$, i.e. every point on this edge is a stationary vortex equilibrium.

It is easy to show that these equilibria are hyperbolic points in the corresponding phase portrait. Thus, the motion from maximum to minimum radii should take infinite time ($T_0 \to \infty$), implying $\delta_{max} \to 0$.

We next estimate the ratio of periods δ_{max} when $\varrho \ll 1$, where analytical progress can be made. The angular velocities remain almost constant in this case, so they can be taken out from under the averaging at the lowest order of approximation, leading to

$$\delta_{max} \approx -\frac{\frac{\gamma R}{\varrho}\mathrm{K}_1(2\gamma\varrho R) + 2\gamma R\mathrm{K}_1(\gamma R) + \frac{1}{2\varrho^2} + 2\cos 2\Phi}{\gamma R\mathrm{K}_1(2\gamma R) + 2\gamma R\mathrm{K}_1(\gamma R) - \frac{3}{2}} - 1. \tag{30}$$

This shows that the period ratio δ_{max} is large, varying from

$$\delta_{max} \approx -\frac{1}{\varrho^2}, \ (\varrho \ll 1,\, R \ll 1,\, -\tilde{M} \ll 1), \tag{31}$$

for small values of R and $-\tilde{M}$, to infinity on the green curve in Fig 3. After crossing this curve, the ratio δ_{max} decreases to the limit value

$$\delta_{max} \approx \frac{1}{3\varrho^2}, \ (\varrho \ll 1,\, \varrho R \gg 1,\, -\tilde{M} \gg 1). \tag{32}$$

We summarise these findings as follows.

I. Above the green curve in Fig. 3, the period ratio δ_{max} decreases from infinity and reaches a minimum in the vicinity of the boundary between the $[-/+]$ and $[-\mathbf{0}+/+]$ regions. For fixed ϱ, the ratio δ_{max} first monotonically increases to infinity with $-\tilde{M}$ then monotonically decreases after crossing the green curve. It decreases to 0 at the edge of the $[\infty]$ region, or to a finite value when $\varrho < 0.414$ (the thin vertical line in Fig. 3).

II. If $\tilde{M} < -0.7398$ (the thin horizontal line in Fig. 3), then the ratio δ_{max} monotonically decreases from large values at small ϱ to 0 at the edge of the $[\infty]$ region.

Fig. 6 illustrates the behaviour of δ_{max}, along with $\delta = T_2/T_1$. We see that the qualitative behaviour of the functions δ_{max} and δ is identical.

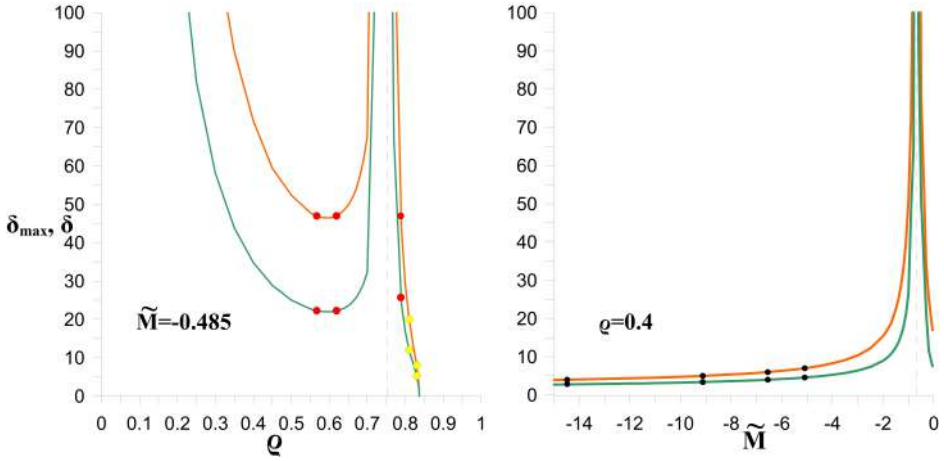

Figure 6: δ_{max} (green) and δ (orange) dependencies on ϱ for a fixed value of $\tilde{M}$ on the left, and the dependencies on $\tilde{M}$ for a fixed value of ϱ on the right. The 5 pairs of markers in the left panel indicate the values of ϱ, δ and δ_{max} for $\tilde{M} = -0.485$ used for the 5 simulations presented in Figs. 7 (yellow markers) and 8 (red markers). The 4 pairs of black markers in the right panel indicate the values of $\tilde{M}$, δ and δ_{max} for $\varrho = 0.4$ used for the 4 simulations presented in Fig. 9.

4.4 Examples of periodic trajectories: simple absolute choreographies

We next examine the trajectories of the lower and upper-layer vortices presented in panels (a), (b), (d) and (e) in Fig. 4. These trajectories are quasi-periodic and fill two annular regions (one in each layer) as $t \to \infty$. Exceptionally, when the period ratio δ_{max} takes integer values (however large), the trajectories become periodic. Fig. 7 presents two examples of such periodic trajectories for $\tilde{M} = -0.485$.

Three more examples, all having the same value of $\tilde{M} = -0.485$ and the same ratio $\delta_{max} = 47$, are shown in Fig. 8. Both vortices in the upper layer make 47 complete oscillations during the period of rotation around the origin, moving along a common trajectory, in all three cases. In panels (a) and (b), they move anticyclonically (typical of the $[-/+]$ region) while in panels (c) they move cyclonically and exhibit a loop-like motion (typical of the region $[-\mathbf{0}+/+]$).

Let us note a curious analogy: the trajectories of the external vortices in Figs. 7 and 8(c) qualitatively resemble the apparent trajectories of Jupiter and Saturn for an Earth-based observer [55].

The periodic trajectories in Fig. 7 and 8 are all for the same value of $\tilde{M} = -0.485$. Qualitatively similar results are obtained by instead keeping ϱ fixed and varying $\tilde{M}$, as shown in Fig. 9. Notably, when δ_{max} is an even integer, the trajectories in the lower layer are relatively simple. The upper-layer vortices move in a nearly circular orbit, only weakly perturbed by the lower-layer ones.

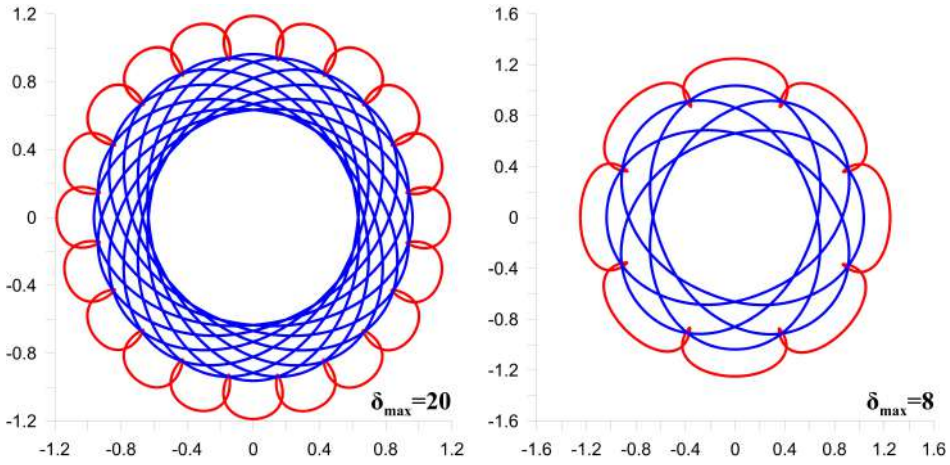

Figure 7: Periodic trajectories for (left) $\delta_{max} = 20$ (having $\delta = 12.061$ and $\varrho = 0.8103$) and (right) $\delta_{max} = 8$ (having $\delta = 5.267$ and $\varrho = 0.8301$). Both have $\tilde{M} = -0.485$. These simulations are indicated by the two pairs of yellow markers on the green and orange curves in the left panel of Fig. 6 (on the curves to the right of the asymptote). They are also indicated by the right closely-spaced pair of grey markers on the horizontal dashed line inside the $[-\mathbf{0}+/+]$ region, close to the edge of the $[\infty]$ border in Fig. 3.

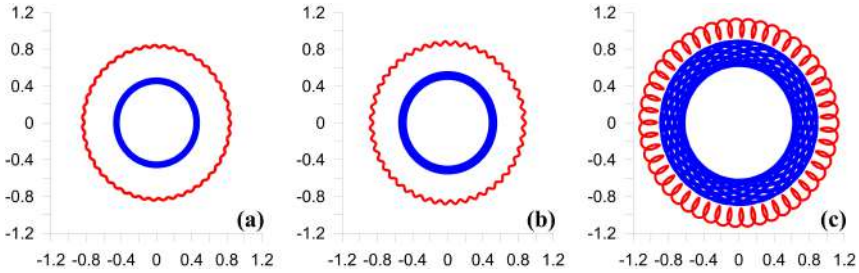

Figure 8: Periodic trajectories for $\tilde{M} = -0.485$ and $\delta_{max} = 47$: (a) $\varrho = 0.5669$, $R = 0.8454$, $\delta = 22.2790$, (b) $\varrho = 0.6189$, $R = 0.8866$, $\delta = 22.2790$; and (c) $\varrho = 0.7881$, $R = 1.1314$, $\delta = 25.7064$. The three pairs of red markers on the green and orange curves in the left panel of Fig. 6 correspond to these simulations. Two of them lie on the left and right branches of the smooth curves to the left of the asymptote, while the third pair lies to the right of the asymptote. In Fig. 3, these simulations correspond to the three grey markers on the dashed line $\tilde{M} = -0.485$, two of which lie in the $[-/+]$ region and one in the $[-\mathbf{0}+/+]$) region.

All the trajectories discussed in this section belong to the category of *simple absolute choreographies*. Both vortices of each layer follow each other along a common trajectory.

4.5 Examples of absolute and relative complex choreographies. General properties of localized regimes.

The points on the green curve in the $[-\mathbf{0}/+]$ region in Fig. 3 correspond to a continuum family of complex absolute choreographies, which now exhibit a quasi-elliptic common trajectory for the two lower layer vortices and two separate closed peripheral curves for the upper layer vortices.

The left part of Fig. 10 shows the entire set of trajectories for 6 separate simulations. The pair of green curves in the figure corresponds to the reference case $(\tilde{M}, \Omega) = (0.754, -0.485)$ already shown in Fig. 4(c). As ϱ^+ decreases, the trajectories of the lower-layer vortices

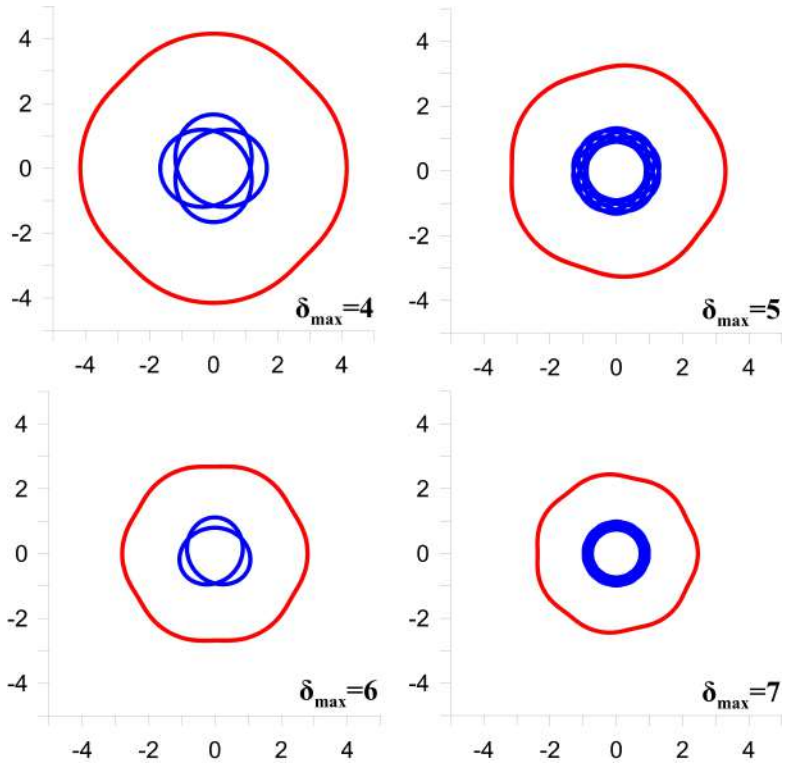

Figure 9: Periodic trajectories at $\varrho = 0.4$, from upper left to lower right: $\delta_{max} = 4$ ($\delta = 2.8145$, $\tilde{M} = -14.480$, $R = 4.1519$); $\delta_{max} = 5$ ($\delta = 3.4032$, $\tilde{M} = -9.125$, $R = 3.2959$); $\delta_{max} = 6$ ($\delta = 4.0127$, $\tilde{M} = -6.560$, $R = 2.7946$); and $\delta_{max} = 7$ ($\delta = 4.5769$, $\tilde{M} = -5.097$, $R = 2.4633$). The four pairs of black markers on the green and orange curves in the right panel of Fig. 6 correspond to these simulations.

uniformly narrow, and the vortices always rotate cyclonically around the origin.

The upper-layer vortex motion is more complicated: for the larger values of ϱ^+, the trajectories are closed curves with a high-curvature tip directed inward toward the origin. Vortices also rotate cyclonically here, due to the strong influence of the lower-layer vortices (this type of motion is similar to that shown previously in Fig. 5 for the vortex coordinates as a function of time). As ϱ^+ decreases further, the following changes successively occur in the vicinity of the high-curvature tip:
(1) a point of self-intersection appears, and the second cell of a doubly-connected figure of 8-shaped trajectory is formed to its left (along which vortices move anticyclonically);
(2) the left cell increases in area while the original (i.e. right one) decreases (this is seen in the deep-blue and violet curves in the bottom right inset);
(3) the original cell disappears completely and only the second one remains (purely anticyclonic motion), now with the tip of high curvature directed outward from the origin (yellow curve).
It is worth noting that these features are only visible when the x and y scales are strongly stretched (more than 10 times in x and 240 times in y).

In the limit $\varrho^+ \to 0$, the vortices in the lower layer merge into a single vortex with strength 2κ, and the upper-layer trajectories degenerate into 2 fixed peripheral points [67]. This limits to a steady baroclinic tripole.

In a sense, the set of complex absolute choreographies in Fig. 10 is universal in an appropriately-rotating frame. One can always find an external rotation rate Ω, for each ϱ^+ and $\tilde{M}$, such that the aperiodic (or quasi-periodic) solutions become periodic. So, if one

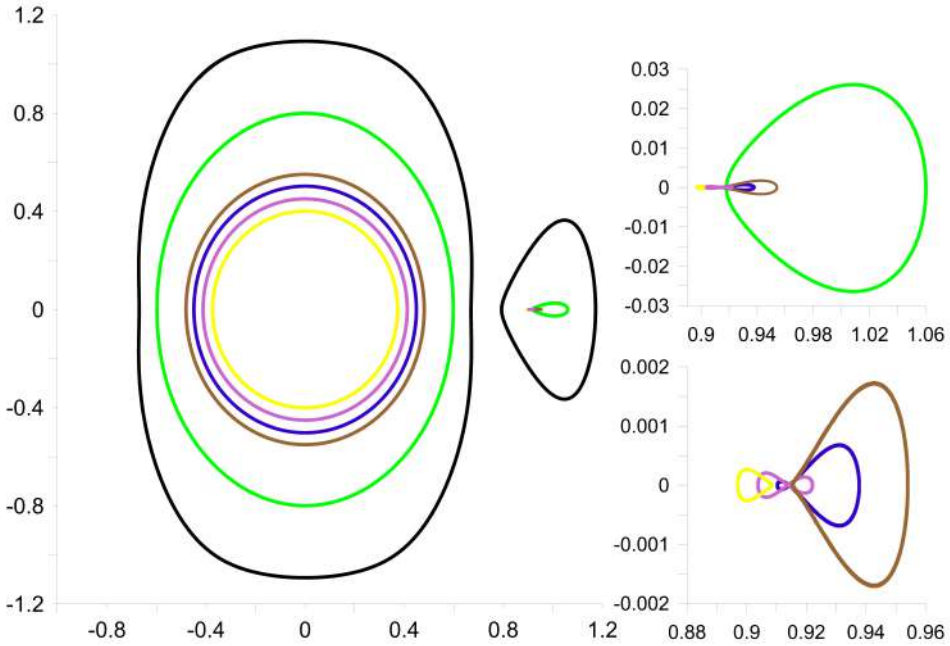

Figure 10: A family of absolute choreographies for a set of parameters $(\varrho^+, \tilde{M})$ indicated by the markers on the green line in Fig. 3. Here we have abandoned the traditional colours. Each colour — from black to yellow — corresponds to a pair of vortices of the upper and lower layers belonging to one virtual heton. On the left is a general view of the choreographies for 6 cases with $(\varrho^+, \tilde{M})$ = (0.9322, -0.180), (0.7540, -0.485), (0.5771, -0.607), (0.5357, -0.627), (0.4889, -0.647) and (0.4410, -0.665). The upper right inset shows a zoom of the upper-layer trajectories for the last 5 cases (in the zoom x is multiplied by 5.7 and y by 16). The bottom right inset shows a further zoom, for the last 4 cases (x is multiplied by 13.8 and y by 242.8).

takes $\Omega = -\langle\dot{\varphi}_1\rangle$, we can ensure $\delta_{max} \to \infty$ in (29). In other words, the absolute choreographies in Figs. 4(c) and 10 are special cases of a wider family of relative choreographies (as defined by Simó in [59]). This is exactly what the Figs. 11 – 13 demonstrate. One can determine how the external parameters of the problem affect the structure of choreographies from these figures.

Fig. 11 examines how the vortex trajectories vary with $\tilde{M}$ while keeping ϱ^+ fixed at 0.754. In each case, the external rotation is taken to be $\Omega = -\langle\dot{\varphi}_1\rangle$ so that the trajectories appear periodic in this rotating frame. The initial conditions for these simulations in the plane $(\varrho^+, \tilde{M})$ are indicated in Fig. 3 by the markers on the short vertical line segment which intersects the green line at the point $(\varrho^+, \tilde{M}) = (0.754, -0.485)$. Here, the deep-blue and brown pairs of curves are the relative choreographies for the absolute trajectories in Fig. 4(a) and Fig. 4(e), correspondingly, and the pair of green lines again shows the reference choreography. The left part of the Fig. 11 and the upper right inset show that with increasing $|\tilde{M}|$ (at least within the interval considered here), the sizes of the closed trajectories for the lower layer increase both in the x-direction and in the y-direction, while for the upper layer they increase in the x-direction, but are non-monotonic in the y-direction.

As shown in the bottom right insert of Fig. 11, the external rotation Ω monotonically increases with decreasing $|\tilde{M}|$, crossing through zero at $\tilde{M} = -0.485$ for the reference case.

Fig. 12 shows the relative choreographies, now for a fixed value of $\Omega = -0.10034$, which is equal to the minimum angular velocity of external rotation in the previous set of simulations. These simulations correspond to the markers on the weakly sloping blue curve in the yellow [+/+] region of Fig. 3. A comparison with the case of absolute choreographies (Fig. 10 where

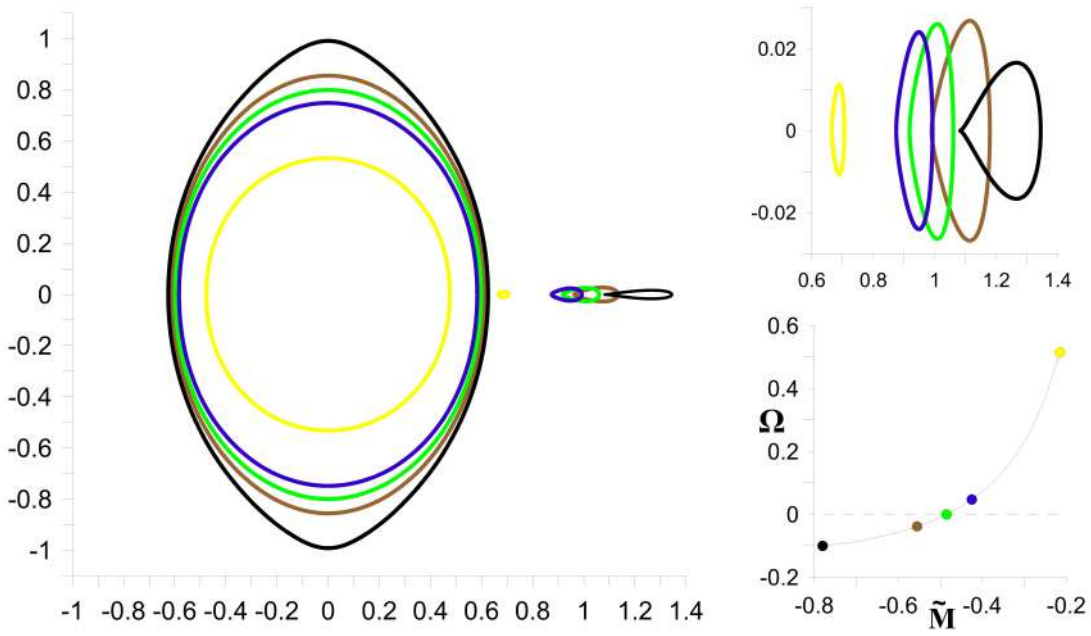

Figure 11: A family of relative choreographies having a fixed value of $\varrho^+ = 0.754$, for 5 pairs of values $(\tilde{M}, \Omega)$ = (-0.215, 0.51543), (-0.425, 0.04723), (-0.485, 0.0000), (-0.555, -0.03834) and (-0.780, -0.10034) (from yellow to black lines, correspondingly). The upper right inset shows a zoom of the upper-layer vortex's trajectories (in the zoom x is multiplied by 1.2 and y by 16.4). The lower right inset shows the dependency $\Omega(\tilde{M})$.

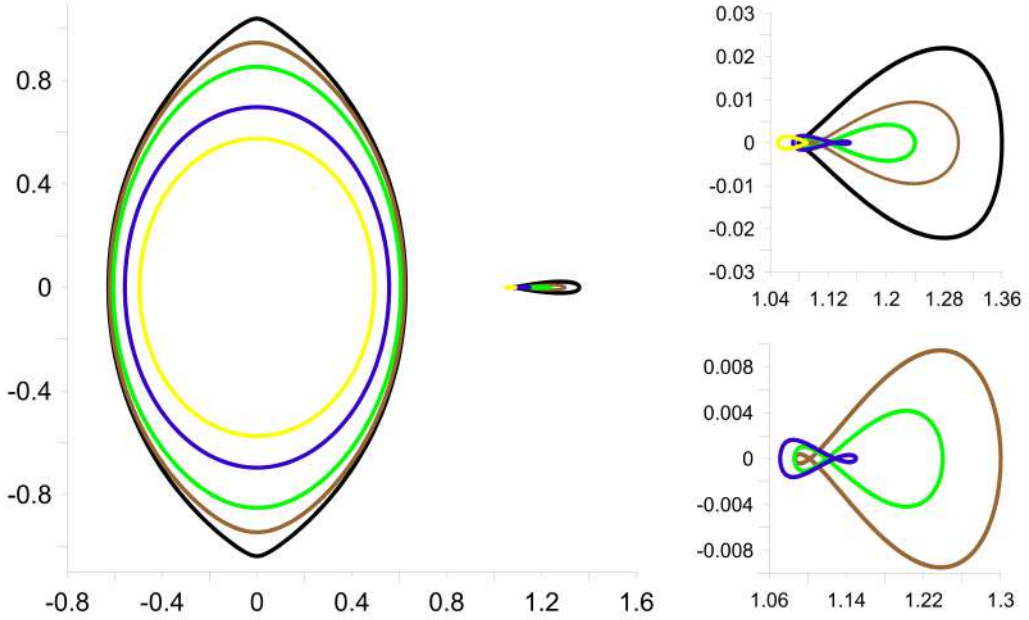

Figure 12: A family of relative choreographies having a fixed value of $\Omega = -0.10034$, for 5 pairs of values $(\varrho^+, \tilde{M})$ = (0.754, -0.780), (0.728, -0.795), (0.687, -0.811), (0.636, -0.828) and (0.570, -0.847). The upper right inset shows a zoom of the upper-layer vortex's trajectories (in the zoom x is multiplied by 2.8 and y by 19.9). The bottom right inset shows a further zoom focusing only on the three figure of 8-shaped trajectories (x is multiplied by 3.7 and y by 50).

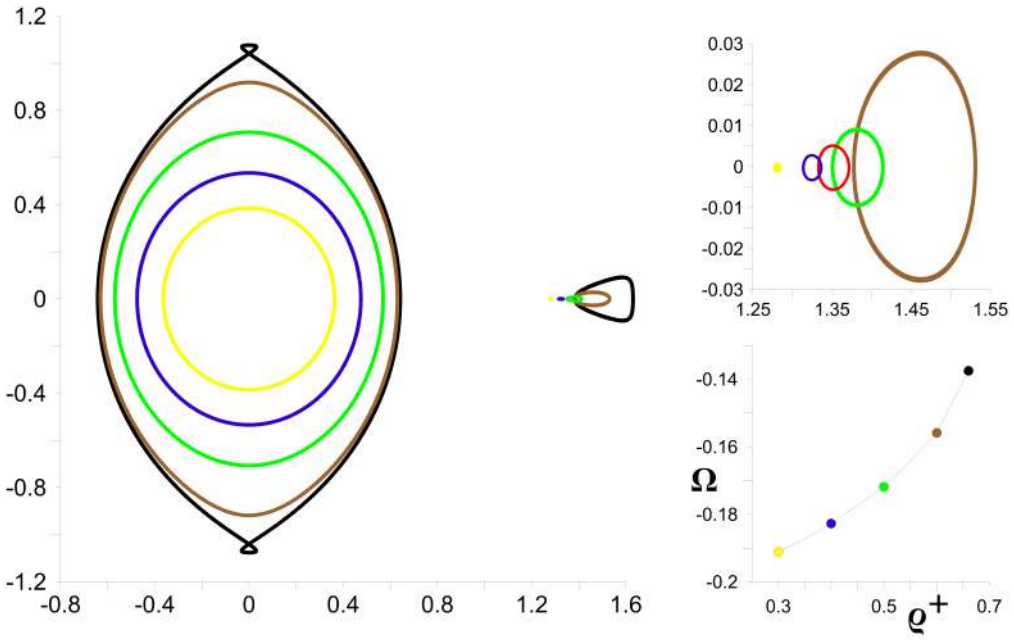

Figure 13: A family of relative choreographies having a fixed value of $\tilde{M} = -1.5$, for 5 pairs of values (ϱ^+, Ω) = (0.6602, -0.1375), (0.604, -0.1559), (0.50, -0.1719),(0.40, -0.1827) and (0.30, -0.1914). The upper right inset shows a zoom of the upper-layer vortex trajectories for last 4 cases (in the zoom x is multiplied by 3.4 and y by 17.4). The bottom right inset shows the dependency $\Omega(\varrho^+)$.

$\Omega = 0$) shows their qualitative similarity. However, there are quantitative differences:
(1) the y extent of the figure of 8-shaped trajectories of the upper layer vortices is now much larger (about 5 times);
(2) naturally, this property is also observed in the lower-layer choreographies;
(3) the area of existence in the space of variables $(\varrho^+, \tilde{M})$ is also now much larger than in the case of absolute choreographies.

A final set of simulations is examined in Fig. 13, now for fixed angular momentum $\tilde{M} = -1.5$. These simulations correspond to the markers on the brown horizontal line in the [+/+] region of Fig. 3. In this set of cases (for sufficiently large $\tilde{M}$), the external (upper-layer) vortices move cyclonically along closed trajectories for all ϱ^+. The following features are noteworthy:
(1) as in Figs. 10 and 12, all the trajectories narrow (in x) as the parameter ϱ^+ decreases;
(2) $\Omega(\varrho^+)$ monotonically increases with ϱ^+, similar to the behaviour of $\Omega(\tilde{M})$ in Fig. 11;
(3) loop-like structures appear in both the external and internal (upper and lower-layer) choreographies. The latter occurs in a very narrow neighbourhood of the border separating the [+/+] and [∞] regions.

The examples of relative choreographies in Figs. 11 – 13, constructed for the fixed parameters ϱ^+, Ω and $\tilde{M}$, respectively, illustrate the universal forms they take for any localized absolute trajectories of the vortices.

We next discuss some general properties of localized, bounded motions with reference to the example presented in Fig. 14. First of all, angular momentum conservation has a geometric interpretation: there is a right-angled triangle of hypotenuse $r_1(t)$, and sides lengths $r_2(t)$ and $\sqrt{-\tilde{M}}$, the latter being constant. Thus, r_1 and r_2 must increase and decrease simultaneously, and in particular, must simultaneously reach their extremal values (this is shown in the lower right panel). We call the period of motion the time between

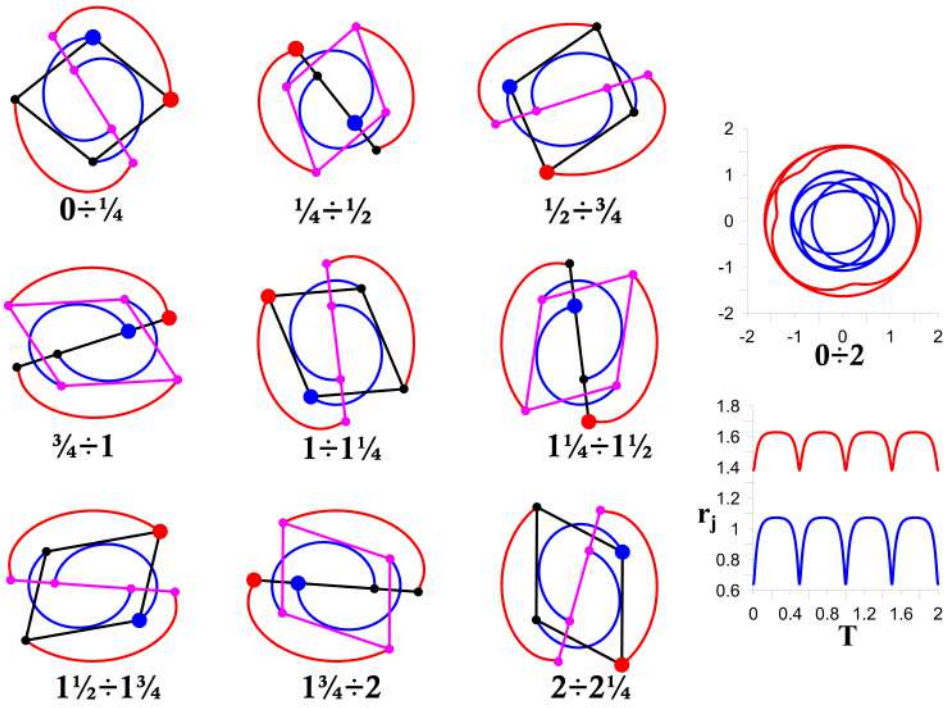

Figure 14: Illustration of the vortex motion over quarter periods as indicated, for $(\tilde{M}, \varrho^+) = (-1.5, 0.6602)$. The left part of the figure shows a set of trajectory sections (here, again we use red for the upper layer and blue for the lower layer) of all four vortices, every quarter period. The vortices successively exhibit rhomboidal and co-linear projections. Large red and blue markers correspond to the upper and lower-layer vortices of the equivalent heton at the initial moment for each panel. Small markers belong to the rest of the vortices and have the colour of the geometric figures on which they lie. In each panel, the initial shape is black, and the final one is purple. The upper right panel shows the absolute vortex trajectories of the equivalent heton over a time interval of two periods. The lower right panel shows $r_1(t)$ and $r_2(t)$ for the equivalent heton over the same time interval.

successive extrema. If the initial projection of the vortex structure is rhomboidal, it is restored twice during the period and passes through a co-linear structure twice. The upper right panel of Fig. 14 shows the vortex trajectories of the equivalent heton over the full two periods. This shows that the trajectories are not closed. In general, as $t \to \infty$, the vortex trajectories fill two concentric annular regions between the extrema in r_1 and r_2.

The phased alternation of extreme (rhomboidal and co-linear) structures every quarter period occurs here because of the 1:2 lower to upper-layer period ratio (as measured by successive extrema in r_1 and r_2). Note that the large red marker advances through half the angular difference of the large blue marker every quarter period. This synchronous periodicity is only exhibited by the radial variables in general, as discussed above.

4.6 Examples of unbounded motion

Thus far we have only considered examples in which the vortices move in annular rings, which is generic for bounded motion. We next consider various scenarios leading to unbounded motion.

We focus on initial conditions taken close to the edge of the $[\infty]$ region in Fig. 3. Three cases are contrasted in Fig. 14, corresponding to the tight cluster of points on the brown

horizontal line in Fig. 3 straddling the [+/+] and [∞] regions.

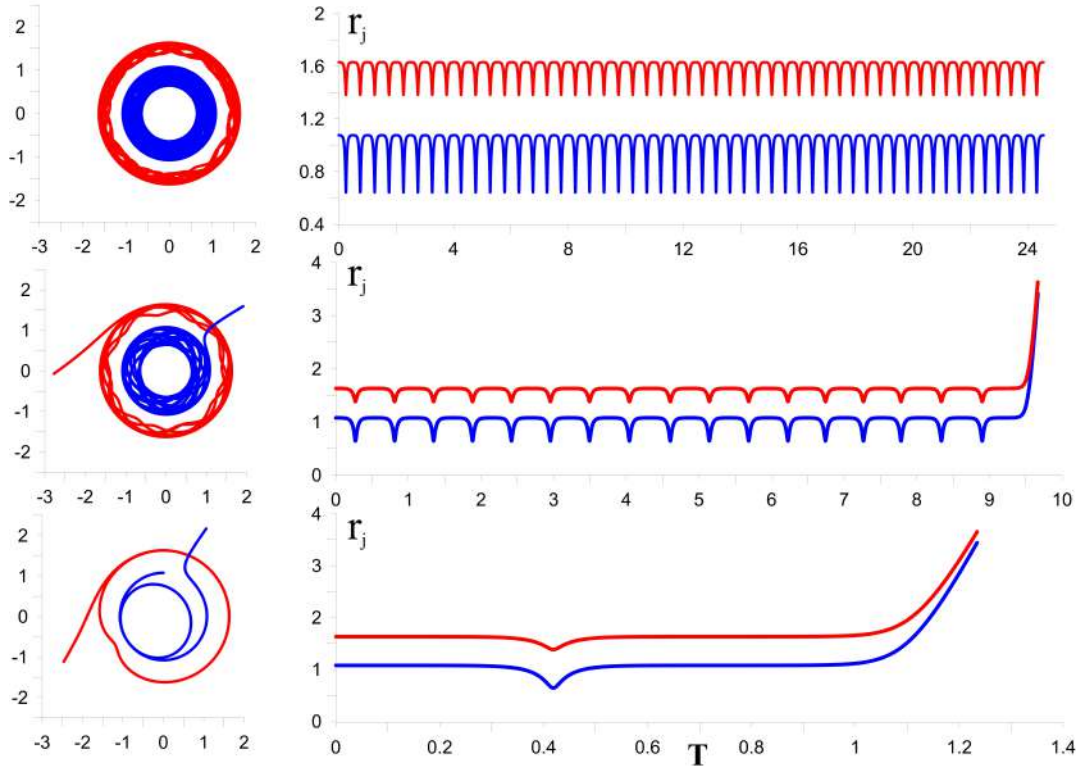

Figure 15: The transition from a localized (bounded) to infinite (unbounded) motion for $\tilde{M} = -1.5$. On the left: upper and lower-layer vortex trajectories for $\varrho^+ = 0.6602$, $\varrho^+ = 0.6603$ and $\varrho^+ = 0.66045$ (top to bottom). On the right: the corresponding time evolution of the radial coordinates $r_j(t)$.

The top row in Fig. 15, where $\varrho^+ = 0.6602$ corresponds to the situation discussed in the previous figure, but here we show the motion for 24 periods (as measured between radial extrema). Over a much longer time, the periodic motion persists. As this initial condition lies just inside the [+/+] region, we expect stability, as observed. However, as the second row in Fig. 15 shows, a very slight increase in ϱ^+, by just 10^{-4}, leads to 'instability'. This initial condition now lies just inside the [∞] region, confirming that vortex trajectories (eventually) diverge. Here it takes 9 periods before this happens due to the close proximity of the [+/+] region. A further increase of ϱ^+ to 0.66045 brings the initial condition further within the [∞] region, resulting in a more rapid divergence. Higher ϱ^+ leads to immediate divergence, with hetonic pairs moving away in opposite directions. Note that all three experiments were performed with a constant value $\tilde{M} = -1.5$.

We have so far considered examples starting from a rhomboidal configuration ($\Phi = \pi/2$). In regimes of bounded motion, the vortex structure periodically returns to its initial state, passing through a co-linear configuration, when $\Phi = 0$. Then all 4 vortices lie on line (after projection to a horizontal plane). Thus, we could have started with initial conditions, for the same angular momentum $\tilde{M}$, which are co-linear rather than rhomboidal, and all of the patterns observed so far — for bounded motions — would be the same (apart from a phase offset).

For unbounded motion, the situation is different. The edge of the [∞] region is in fact a bifurcation line. In Fig. 3 the [∞] region corresponds to regimes of scattering for hetonic pairs initially in a rhomboidal configuration. Unstable, initially co-linear, configurations

correspond to another sheet of the plane of the variables $(\tilde{M}, \varrho^-)$[3].

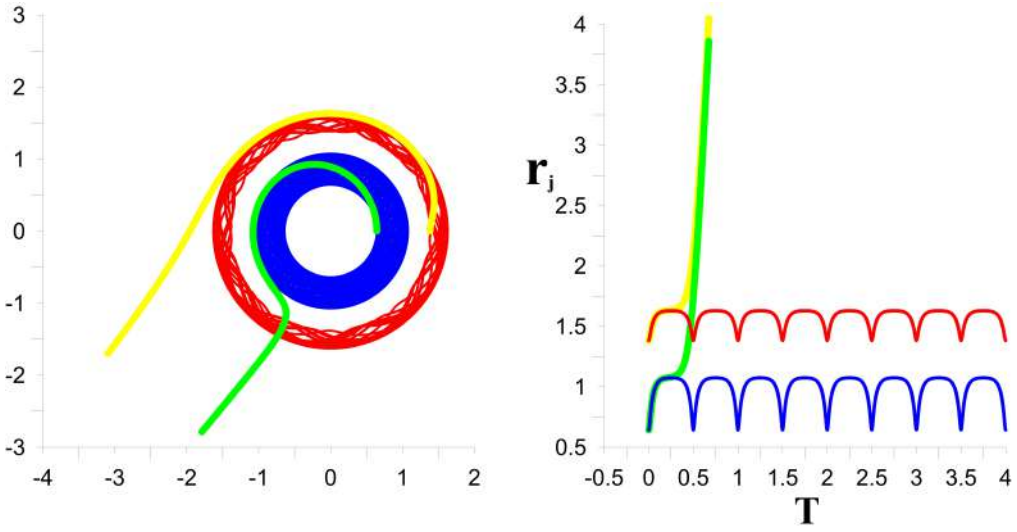

Figure 16: On the left: trajectories of the upper and lower-layer vortices starting from a co-linear state having $\tilde{M} = -1.5$ and $\varrho^- = 0.46443$ (bounded regime, red and blue lines), or $\varrho^- = 0.46444$ (unbounded regime, bold green and yellow lines). On the right: corresponding $r_j(t)$ dependencies.

Fig. 16 shows the trajectories for initially co-linear vortices in two cases corresponding to bounded and unbounded regimes of motion. Note that ϱ^- differs by only 10^{-5} between the cases. The edge of the unbounded regime in ϱ^- corresponds to ϱ^*, the point where the minimum of the Hamiltonian $\mathcal{H}^+$ is reached. In the bounded case, the value of $\varrho^- = 0.46443$ corresponds to $\varrho^+ = 0.66020$ used in the previous simulation (top row in Fig. 15).

4.7 Finite core vortices

We briefly discuss the effect of considering finite core vortices instead of singular (point) ones. For this purpose, we replace the singular vortices by compact, uniform potential vorticity vortex patches. Finite core vortices have a shape and therefore can deform. This deformation has an impact on the dynamics. We conduct a series of simulations using initially circular patches of radius $r_v = 0.2$, and of potential vorticity $q = \pm 2\pi$. In this way, each patch has a strength $\pm\kappa$ with $\kappa = \iint_{vortex} q dV = 2(\pi/5)^2$. The influence of finite size on the flow evolution will be discussed in depth in a companion paper. Here we simply give a flavour of what may be expected, and in particular demonstrate that the trajectories of finite core vortices can be similar to those of point vortices.

We consider $\varrho^+ = 0.754$ as in the point vortex simulations shown in Fig. 11. Recall that for this value of ϱ^+, the periodic solution is obtained for $\tilde{M} = -0.485$. Numerical experiments show that for finite core vortices of radius $r_v = 0.2$, the periodic solution is obtained for a nearby value $\tilde{M} = -0.4988$. Fig. 17 shows the trajectories and a snapshot of the vortices in three simulations having $\tilde{M} = -0.450$, -0.4988 and -0.550 respectively, over the time interval for $0 \le t \le 1550$. We also plot in the figure the trajectories of the equivalent point vortices.

[3] In the particular case $\tilde{M} = 0$, when the initial rhombus becomes a square, the corresponding bifurcations occur in the vicinity of the hyperbolic points of the phase portrait [31, 68].

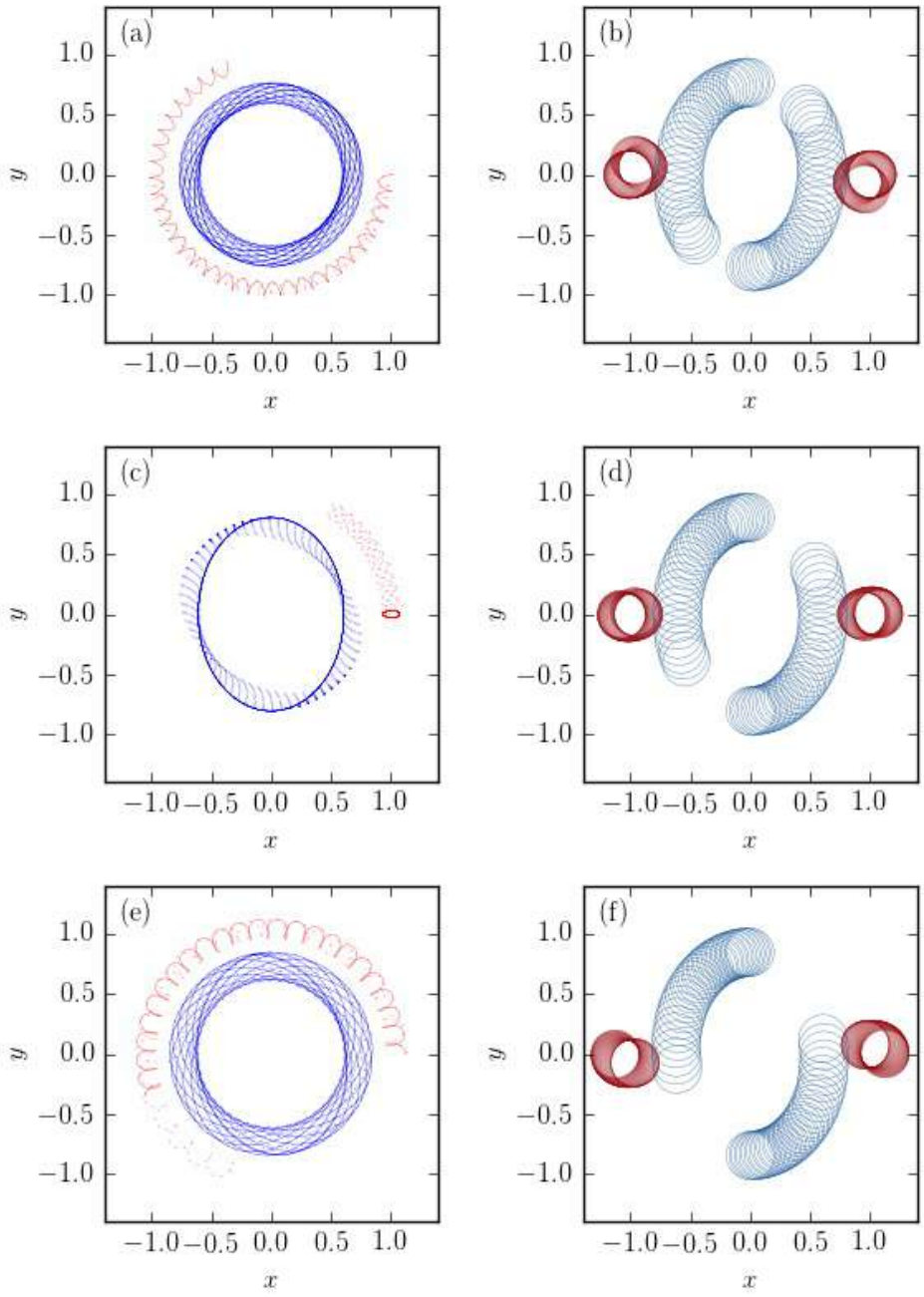

Figure 17: Trajectories of one upper-layer and one lower-layer vortex (the equivalent heton) for $\varrho^+ = 0.754$ and (a) $\tilde{M} = -0.450$, (c) -0.4988 and (e) -0.550, for $0 \leq t \leq 1550$ with $\kappa = 2 * (\pi/5)^2$: solid lines correspond to the finite core vortices with $r_v = 0.2$ while dotted lines correspond to the point vortices (dotted lines). Projected top view of the finite core vortices for $0 \leq t \leq 35$ for (b) $\tilde{M} = -0.450$ (d) -0.4988 and (f) -0.550. The vortex bounding contours are drawn every $\Delta t = 1$.

There is generally good agreement between the trajectories of the point vortices and the finite core ones. It should be noted that in these three cases, at $t = 0$, the inner radii $r_1 = 1.02, 1.08, 1.13$ and the outer radii $r_2 = 0.77, 0.81, 0.85$ for $\varrho^+ = 0.754$ and $\tilde{M} = -0.450, -0.4988$ and -0.550, respectively. Hence $r_v/r_1 \sim 0.18 - 0.2$ in all cases; i.e. the vortices are relatively compact. The main difference is quantitative — a slightly larger value of $\tilde{M}$ is required to obtain an (approximately) periodic solution (modulo additional shape variations). This is due to the fact that, for $\tilde{M} = -0.450$, the external finite core vortices travel faster in the cyclonic direction than their point vortex counterparts, while they travel slower in the anticyclonic direction for $\tilde{M} = -0.550$. Nonetheless, it is expected that, so long as the deformation of the finite core vortices remains small, all conclusions reached for the point vortex dynamics are also valid for the finite core dynamics.

5 Discussion and concluding remarks

The concept of hetons, baroclinic vortices with zero total strength (integrated potential vorticity), introduced originally by Hogg and Stommel in [31], has inspired a wide range of studies into the dynamics of hetons and their interactions. Moreover, many problems can be thoroughly and consistently studied within the framework of the quasi-geostrophic theory of discrete (point) vortices.

In this paper, we have examined the general motion of N hetons with N-fold symmetry in the two-layer quasi-geostrophic model. The imposed symmetry reduces the original system of $4N$ ordinary differential equations governing the motion of the discrete vortices to a system of just 4 equations for the polar coordinates of an equivalent heton. Using angular momentum conservation and the fact that the equations depend only on the angular differences between the vortices, we can further reduce the system to two equations for the so-called 'virtual vortex'. These equations, as well as the expression for the Hamiltonian, are valid for any N.

We have carried out a detailed analysis for the special case of $N = 2$ hetons. All results were obtained assuming the vortex strengths κ are positive in the lower layer, and negative in the upper one. Changing the sign of κ merely changes the direction of rotation of the vortices. We have also assumed that the lower to upper-layer radius ratio $\varrho = r_2/r_1 < 1$. However, the results for $\varrho > 1$ are identical upon interchanging the layers. These symmetries are inherited from the governing quasi-geostrophic model.

We have paid special attention to the study of bounded, and in particular, periodic motion. We have shown that among the continuum of possible finite motions, one can find a countable number of periodic ones. We have found classes of absolute and relative 'choreographies'. Recall that the term 'choreography' was first introduced by Simó in [59] to qualify the periodic motion of material points moving along a common closed trajectory. Such structures appear in different problems of celestial mechanics [3,13,14]. The concept of choreography for vortices on a plane and on a sphere was used for the first time by Borisov et al in [4,5]. For vortices in a two-layer and three-layer rotating fluid, choreographies have been studied in [63,64,66–68]. The current understanding the problem, from a rigorous mathematical point of view, is given in works [6,7,15].

While the problem studied herein is idealised, it is relevant to oceanic heat and mass transport. This is especially true of the unbounded 'scattering' type motions examined. We have identified the portion of parameter space where this occurs, which is essentially delineated by the system's angular momentum and energy (or Hamiltonian). A related question, to be examined in a future study, is the stability of the symmetric hetonic configurations to perturbations which break the N-fold symmetry. Furthermore, in the nonlinear dynamics,

can two (or generally N) hetons become 'trapped' in a portion of the plane? Is this determined by the conserved invariants of angular momentum and energy? We hope to report on this in the near future.

Acknowledgements This work was carried out as part of a joint project funded by the Russian Foundation for Basic Research (grant 20-55-10001) and UK Royal Society (grant IEC\R2\192170). MAS was also supported by the program 0147-2019-0001 (State Registration No. AAAA-A18-118022090056-0) and by the Ministry of Science and Education of the Russian Federation (Project No. N14.W03.31.0006), KVK was supported by RFBR project No. 20-05-00083.

The authors gratefully acknowledge anonymous Reviewers for constructive and helpful comments.

The data that support the findings of this study are available from the corresponding author upon reasonable request.

References

[1] Aref, H. 1982. Point vortex motions with a center of symmetry. Phys. Fluids. 25(12), 2183–2187.

[2] Aref, H., Stremler, M.A. 1999. Four-vortex motion with zero total circulation and impulse. Phys. Fluids. 11(12), 3704–3715.

[3] Barutello, V., Terracini, S. 2004. Action minimizing orbits in the n-body problem with simple choreography constraint. Nonlinearity. 17(6), 2015–2039.

[4] Borisov, A.V., Mamaev, I.S., Kilin, A.S. 2004. Absolute and relative choreographies in the problem of point vortices moving on a plane. Regul. Chaotic Dyn. 9(2), 101–111.

[5] Borisov, A.V., Mamaev, I.S., Kilin, A.A. 2005. New periodic solutions for three or four identical vortices on a plane and a sphere. Discrete Contin. Dyn. Syst., suppl., 110–120. DOI:10.3934/proc.2005.2005.110.

[6] Calleja, R.C., Doedel, E.J., García-Azpeitia, C. 2018. Choreographies in the n-vortex problem. Regul. Chaotic Dyn. 23(5), 595–612.

[7] Calleja, R., Doedel, E., García-Azpeitia, C., Pando, C. 2018. Choreographies in the discrete nonlinear Schrödinger equations. Eur. Phys. J. Special Topics. 227(5-6), 615–624.

[8] Chao, S.-Y., Shaw, P.-T. 1998. Eddy maintenance and attrition in a vertically sheared current under Arctic ice. J. Phys. Oceanogr. 28(12), 2427–2443.

[9] Chao, S.-Y., Shaw, P.-T. 1999. Close interactions between two pairs of heton-like vortices under sea ice. J. Geophys. Res. 104(C10), 23591–23605.

[10] Chao, S.-Y., Shaw, P.-T. 1999. Fission of heton-like vortices under sea ice. J. Oceanogr. 55(1), 65–78.

[11] Chao, S.-Y., Shaw, P.-T. 2000. Slope-enhanced fission of salty hetons under sea ice. J. Phys. Oceanogr. 30(11), 2866–2882.

[12] Chao, S.-Y., Shaw, P.-T. 2003. Heton shedding from submarine-canyon plumes in an Arctic boundary current system: Sensitivity to the undercurrent. J. Phys. Oceanogr. 33(9), 2032–2044.

[13] Chenciner, A., Gerver, J., Montgomery, R., Simó, C. 2001. Simple choreographies of N bodies: a preliminary study. In: *Geometry, Mechanics, and Dynamics. Volume in honor of the 60th birthday of J. E. Marsden* (Eds. P. Newton, P. Holmes, A. Weinstein). Springer, New York, NY, 287–308.

[14] Chenciner, A., Montgomery, R. 2000. A remarkable periodic solution of the three-body problem in the case of equal masses. Ann. Math. 152(3), 881–901.

[15] Dai, Q., Gebhard, B., Bartsch, T. 2018. Periodic solutions of N-vortex type Hamiltonian systems near the domain boundary. SIAM J. Appl. Math. 78(2), 977–995.

[16] DiBattista, M.T., Majda, A.J. 2000. An equilibrium statistical theory for large-scale features of open-ocean deep convection. J. Phys. Oceanogr. 30(6), 1325–1353.

[17] Fernando, H.J.S., Chen, R., Ayotte, B.A. 1998. Development of a point plume in the presence of background rotation. Phys. Fluids, 10(9), 2369–2383.

[18] Fernando, H.J.S., Smith IV D.C. 2001. Vortex structure in geophysical convection. Eur. J. Mech. B/Fluids, 20(4), 437–470.

[19] Griffiths, R.W., Hopfinger, E.J. 1986. Experiments with baroclinic vortex pairs in a rotating fluid. J. Fluid Mech. 173, 501–518.

[20] Griffiths, R.W., Hopfinger E.J. 1987. Coalescing of geostrophic vortices. J. Fluid Mech. 178, 73–97.

[21] Gryanik, V.M. 1983. Dynamics of singular geostrophic vortices in a two-level model of atmosphere (ocean). Izvestiya, Atmos. Ocean. Phys. 19(3), 171–179.

[22] Gryanik, V.M. 1983. Dynamics of localized vortex perturbations 'vortex charges' in a baroclinic fluid. Izvestiya, Atmos. Ocean. Phys. 19(5), 347–352.

[23] Gryanik, V.M. 1988. Localized vortices - 'vortex charges' and 'vortex filaments' in a baroclinic differentially rotating fluid. Izvestiya, Atmos. Ocean. Phys. 24(12), 919–926.

[24] Gryanik, V.M., Borth, H., Olbers, D. 2001. The theory of quasigeostrophic von Kármán vortex streets in two-layer fluids on beta-plane and intermittent turbulent jets. Alfred-Wegener-Institut für Polar- und Meeresforschung, Preprint 106, 59 pp.

[25] Gryanik, V.M., Borth, H., Olbers, D. 2004. The theory of quasigeostrophic von Kármán vortex streets in two-layer fluids on beta-plane. J. Fluid Mech. 505, 23–57.

[26] Gryanik, V.M., Doronina, T.N. 1990. Advective transport of a conservative solute by baroclinic singular quasigeostrophic vortices in the atmosphere (ocean). Izvestiya, Atmos. Ocean. Phys. 26(10), 1011–1026.

[27] Gryanik, V.M., Doronina, T.N., Olbers, D., Warncke, T.H. 2000. The theory of three-dimensional hetons and vortex-dominated spreading in localized turbulent convection in a fast rotating stratified fluid. J. Fluid Mech. 423, 71–125.

[28] Gryanik, V.M., Sokolovskiy, M.A., Verron, J. 2006. Dynamics of heton-like vortices. Regul. Chaotic Dyn. 11(3), 417–438.

[29] Helfrich, K.R., Battisti, T.M. 1991. Experiments on baroclinic vortex shedding from hydrothermal plumes. J. Geophys. Res., 96(C12), 12,511–12,518.

[30] Helfrich, K.R., Send, U. 1988. Finite-amplitude evolution of two-layer geostrophic vortices. J. Fluid Mech. 197, 331–348.

[31] Hogg, N.G., Stommel, H.M. 1985. The heton, an elementary interaction between discrete baroclinic geostrophic vortices, and its implications concerning eddy heat-flow. Proc. Roy. Soc. London A, 397, 1–20.

[32] Hogg, N.G., Stommel, H.M., 1985. Hetonic explosions: the breakup and spread of warm pools as explained by baroclinic point vortices. J. Atmos. Sci. 42(14), 1465–1476.

[33] Hogg, N.G., Stommel, H.M. 1990. How currents in the upper thermocline could advect meddies deeper down. Deep Sea Res. 37(4), 613–623.

[34] Jamaloodeen, M.I., Newton, P.K. 2007. Two-layer quasigeostrophic potential vorticity model. J. Math. Phys. 48(6), 065601. DOI:0.1063/1.2469221.

[35] Kizner, Z. 2006. Stability and transitions of hetonic quartets and baroclinic modons. Phys. Fluids. 18(5), 056601. DOI:10.1063/1.2196094.

[36] Klinger, B.A., Marshall, J. 1995. Regimes and scaling laws for rotating deep convection in the ocean. Dyn. Atmos. Oceans. 21, 221–256.

[37] Koshel, K.V., Reinaud, J.N., Riccardi, G., Ryzhov, E.A. 2018. Entrapping of a vortex pair interacting with a fixed point vortex revisited. I. Point vortices. Phys. Fluids, 30(9), 096603. DOI:10.1063/1.5040884.

[38] Kozlov, V.F., Makarov, V.G., Sokolovskiy, M.A. 1986. Numerical model of the baroclinic instability of axially symmetric eddies in two-layer ocean. Izvestiya, Atmos. Ocean. Phys. 22(8), 674–678.

[39] Legg, S., Jones, H., Visbeck, M. 1996. A heton perspective of baroclinic eddy transfer in localized open ocean convection. J. Phys. Oceanogr. 26(10), 2251–2266.

[40] Legg, S., Marshall, J. 1993. A heton model of the spreading phase of open-ocean deep convection. J. Phys. Oceanogr. 23(6), 1040–1056.

[41] Legg, S., Marshall, J. 1998. The influence of the ambient flow on the spreading of convected water masses. J. Marine Res. 56(1), 107–139.

[42] Legg, S., McWilliams, J., Gao, J. 1998. Localization of deep ocean convection by a mesoscale eddy. J. Phys. Oceanogr. 28(5), 944–970.

[43] Lim, C.C., Majda, A.J. 2001. Point vortex dynamics for coupled surface/interior QG and propagating heton clasters in models for ocean convection. Geophys. Astrophys. Fluid Dyn. 94(3–4), 177–220.

[44] Makarov, V.G., Sokolovskiy, M.A., Kizner, Z. 2012. Doubly symmetric finite-core heton equilibria. J. Fluid Mech. 708, 397–417.

[45] Mokhov, I.I., Gryanik, V.M., Doronina, T.N., Lagun, D.E., Mokhov, O.I., Naumov, E.P., Petukhov, V.K., Tevs, M.V., Khairullin, R.R. 1993. Vortex activity in the atmosphere: tendencies of changes. Moscow: Institute of Atmospheric Physics of RAS, Preprint N 2, 97 pp.

[46] Mokhov, I.I., Doronina, T.N., Gryanik, V.M., Khairullin, R.R., Korovkina, L.V., Lagun, V.E., Mokhov, O.I., Naumov, E.P., Petukhov, V.K., Senatorsky, A.O., Tevs, M.V. 1994. Extratropical cyclones and anticyclones: Tendencies of change. In: *The Life of Extratropical Cyclones: Vol. 2.* (Eds. S. Gronas, M.A. Shapiro). Bergen (Norway): Geophysical Institute, University of Bergen, 56–60.

[47] Morel, Y., McWilliams, J. 2001. Effect of isopycnal and diapycnal mixing on the stability of oceanic currents. J. Phys. Oceanogr. 31(8), 2280–2296.

[48] Pedlosky, J. 1985. The instability of continuous heton clouds. J. Atmos. Sci. 42(14), 1477–1486.

[49] Polvani, L.M. 1991. Two-layer geostrophic vortex dynamics. 2. Alignment and two-layer V-states. J. Fluid Mech. 225, 241–270.

[50] Polvani, L.M., Zabusky, N.J., Flierl, G.R. 1988. Applications of contour dynamics to two-layer quasi-geostrophic flows. Fluid Dyn. Res. 3(1–4), 422–424.

[51] Reinaud, J.N. 2015. On the stability of continuously stratified quasi-geostrophic hetons. Fluid Dyn. Res. 2015, 47, 035510. DOI:10.1088/0169-5983/47/3/035510.

[52] Reinaud, J., Carton, X. 2009. The stability and the nonlinear evolution of quasi-geostrophic hetons. J. Fluid Mech. 636, 109–135.

[53] Reinaud, J.N., Carton, X., Dritschel, D.G. 2017. Interaction between a quasi-geostrophic buoyancy filament and a heton. Fluids. 2, x, doi:10.3390.

[54] Reinaud, J.N., Koshel, K.V., Ryzhov, E.A. 2018. Entrapping of a vortex pair interacting with a fixed point vortex revisited. II. Finite size vortices and the effect of deformation. Phys. Fluids, 30(9), 096604. DOI:10.1063/1.5052202.

[55] Rogers, E.M. 1969. Physics for the Inquiring Mind: Teacher's Book. Oxford University Press. 120 p.

[56] Ryzhov, E.A., Sokolovskiy, M.A. 2016. Interaction of two-layer vortex pair with a submerged cylindrical obstacle in a two-layer rotating fluid. Phys. Fluids. 28, 056602. DOI:10.1063/1.4947248.

[57] Serra, N., Sadux, S., Ambar, I. 2002. Observations and laboratory modeling of meddy generation of cape St. Vincent. J. Phys. Oceanogr. 32(1), 3–25.

[58] Shaw, P.-T., Chao, S.-Y. 2003. Effects of a baroclinic current on a sinking dense water plume from a submarine canyon and heton shedding. Deep Sea Res. Part I. 50(3), 357–370.

[59] Simó, C. 2001. New families of solutions to the N-body problems. In: *Proc. European 3rd Congress of Mathematics*, Vol. I (Barcelona, 2000). (Eds. C. Casacuberta, R.M. Miró-Roig, J. Verdera, S. Xambó-Descamps), *Progr. Math series.*, vol. 201, Birkhäuser, Basel, 101–115.

[60] Sokolovskiy, M.A. 1988. Numerical modelling of nonlinear instability for axisymmetric two-layer vortices. Izvestiya, Atmos. Ocean. Phys. 24(7), 536–542.

[61] Sokolovskiy, M.A. 1989. Head-on collisions of distributed hetons. Trans. Dokl. USSR Acad. Sci, Earth Sci. Sect. 306(3), 215–217.

[62] Sokolovskiy, M.A., Carton, X. 2010. Baroclinic multipole formation from heton interaction. Fluid Dyn. Res. 42, 045501.

[63] Sokolovskiy, M.A., Carton, X.J., Filyushkin, B.N. 2020. Mathematical modeling of vortex interaction using a three-layer quasigeostrophic model. Part 1: Point-vortex approach. Mathematics. 8(8), 1228. DOI:10.3390/math8081228.

[64] Sokolovskiy, M.A., Koshel, K.V., Verron, J. 2013. Three-vortex quasi-geostrophic dynamics in a two-layer fluid. Part I. Analysis of relative and absolute motions. J. Fluid Mech. 717, 232–254.

[65] Sokolovskiy, M.A., Verron, J. 2000. Finite-core hetons: Stability and interactions. J. Fluid Mech. 423, 127–154.

[66] Sokolovskiy, M.A., Verron, J. 2000. Four-vortex motion in the two layer approximation: Integrable case. Regul. Chaotic Dyn. 5(4), 413–436.

[67] Sokolovskiy, M.A., Verron, J. 2002. Dynamics of triangular two-layer vortex structures with zero total intensity. Regul. Chaotic Dyn. 7(4), 435-472.

[68] Sokolovskiy, M.A., Verron, J. 2014. Dynamics of vortex structures in a stratified rotating fluid. Series Atmos. Oceanogr. Sci. Lib. Vol. 47, Springer: Switzerland, 382 p.

[69] Sokolovskiy, M., Verron, J., Carton, X., Gryanik, V. 2010. On instability of elliptical hetons. Theor. Comput. Fluid Dyn. 24(1–4), 117–123.

[70] Sokolovskiy, M.A., Verron, J., Vagina, I.M. 2001. Effect of a submerged small-height obstacle on the dynamics of a distributed heton. Izvestiya, Atmos. Ocean. Phys. 37(1), 122–133.

[71] Thivolle-Cazat, E., Sommeria, J., Galmiche, M. 2005. Baroclinic instability of two-layer vortices in laboratory experiments. J. Fluid Mech. 544, 69–97.

[72] Valcke, S., Verron, J. 1993. On interactions between two finite-core hetons. Phys. Fluids. A5(8), 2058–2060.

[73] Valcke, S., Verron, J. 1996. Cyclone-anticyclone asymmetry in the merging process. Dyn. Atmos. Oceans. 24(1–4), 227–236.

[74] Valcke, S., Verron, J. 1997. Interactions of baroclinic isolated vortices: The dominant effect of shielding. J. Phys. Oceanogr. 27(4), 524–541.

[75] Verron, J., Hopfinger, E. 1991. The enigmatic merging conditions of two-layer baroclinic vortices. C. R. Acad. Sci. Paris Ser. II, 313(7), 737–742.

[76] Verron, J., Hopfinger, E., McWilliams, J.C. 1990. Sensitivity to initial conditions in the merging of two-layer baroclinic vortices. Phys. Fluids, A2(6), 886–889.

[77] Verron, J., Valcke, S. 1994. Scale-dependent merging of baroclinic vortices. J. Fluid Mech. 264, 81–106.

[78] Young, W.R. 1985. Some interactions between small numbers of baroclinic, geostrophic vortices. Geophys. Astrophys. Fluid Dyn. 33(1–4), 35–61.